A fluid inclusion and stable isotope study of the Pebble porphyry copper-gold-molybdenum deposit, Alaska

CrossMark

Melissa J. Gregory

Mineral Deposit Research Unit, Department of Earth, Ocean and Atmospheric Sciences, University of British Columbia, 2020-2207 Main Mall, Vancouver, British Columbia V6T 1Z4, Canada

A B S T R A C T

The hydrothermal fluid evolution in the supergiant Pebble porphyry Cu-Au-Mo deposit in southwest Alaska has been constrained using fluid inclusion and light stable isotope data. The deposit is related to ~90 Ma granodiorite porphyry intrusions and mineralization occurs primarily in sodic-potassic, potassic, and advanced argillic alteration zones.

Throughout the deposit vein quartz hosts intermediate-density fluid inclusion assemblages with an average salinity of 9.5 wt% NaCl equivalent and homogenization temperatures of 377 to 506 °C. Pressure corrections result in trapping temperatures with a maximum of 610 °C. This early fluid exsolved from a crystallizing magma at depth and underwent phase separation under varying conditions during cooling and depressurization forming two distinct fluid compositions. The two fluids formed two hydrothermal alteration assemblages which have different metal signatures. In the hydrothermal core in the eastern part of the system, high-density quartz veins, potassic alteration and the most economically significant mineralization are related to ~52 wt% NaCl equivalent brines that coexist with very low-density vapor. In the western part of the system peripheral to the hydrothermal core, lower quartz vein densities accompanied by sodic-potassic alteration and lower grade mineralization are associated with ~38 wt% NaCl equivalent brines and low-density vapor. Sulfide mineralization precipitated late in this early alteration event at temperatures between 375 and 330 °C.

Fluids related to sodic-potassic alteration minerals have $\delta^{18}O$ signatures from +6.0 to +10.5‰ VSMOW and δD values from −70 to −41‰ VSMOW, which are consistent with a magmatic fluid source. Fluids related to potassic alteration assemblages have $\delta^{18}O$ of −1.7 to +2.3‰ VSMOW and δD of −68 to −59‰ VSMOW, which suggests that the magmatic fluids evolved to lighter oxygen isotope signatures due to quartz precipitation during alteration.

Lower temperature (~280 °C) sericite and illite alteration followed the high-temperature magmatic stage and formed from the rising vapor plume as it mixed with varying amounts of meteoric fluid. Sericite in quartz-sericite-pyrite alteration on the periphery of the deposit and illite from areas of illite ± kaolinite alteration which overprints sodic-potassic alteration and forms quartz-illite-pyrite alteration within the deposit are related to low-salinity aqueous fluids that have a significant magmatic component (+2.1 to +4.1‰ $\delta^{18}O$ and −76 to −67‰ δD). Illite alteration which overprints both potassic alteration and quartz-sericite-pyrite alteration formed from fluids with a large meteoric component (−9.1 to −4.8‰ $\delta^{18}O$ and −101 to −90‰ δD). The higher vein density and therefore higher permeability in the core of the deposit facilitated ingress of larger amounts of meteoric fluid compared with the more peripheral region.

Advanced argillic alteration and associated high-grade mineralization are related to a second pulse of magmatic fluid which did not intersect the two phase field during cooling and depressurization. The fluid contracted to form a 3 wt% NaCl equivalent aqueous fluid that resulted in a sericite-pyrite-bornite-digenite bearing assemblage with a magmatic signature (4.6 to 6.5‰ $\delta^{18}O$ and −108 to −102‰ δD) at 340 °C. Cooling and mixing of this fluid with meteoric water resulted in a fluid that formed a pyrophyllite-quartz-sericite-chalcopyrite bearing assemblage (−8.9 to −0.6‰ $\delta^{18}O$ and −110 to −96‰ δD) at 300 °C. Compared to older potassic and sodic-potassic alteration, the advanced argillic alteration has a highly depleted δD signature which is attributed to degassing of a crystallizing intrusive fluid source.

© 2016 Elsevier B.V. All rights reserved.

1. Introduction

The Pebble porphyry Cu-Au-Mo deposit is located in southwest Alaska (Fig. 1A) and is one of the world's largest concentrations of

E-mail address: melissajgregory@gmail.com.
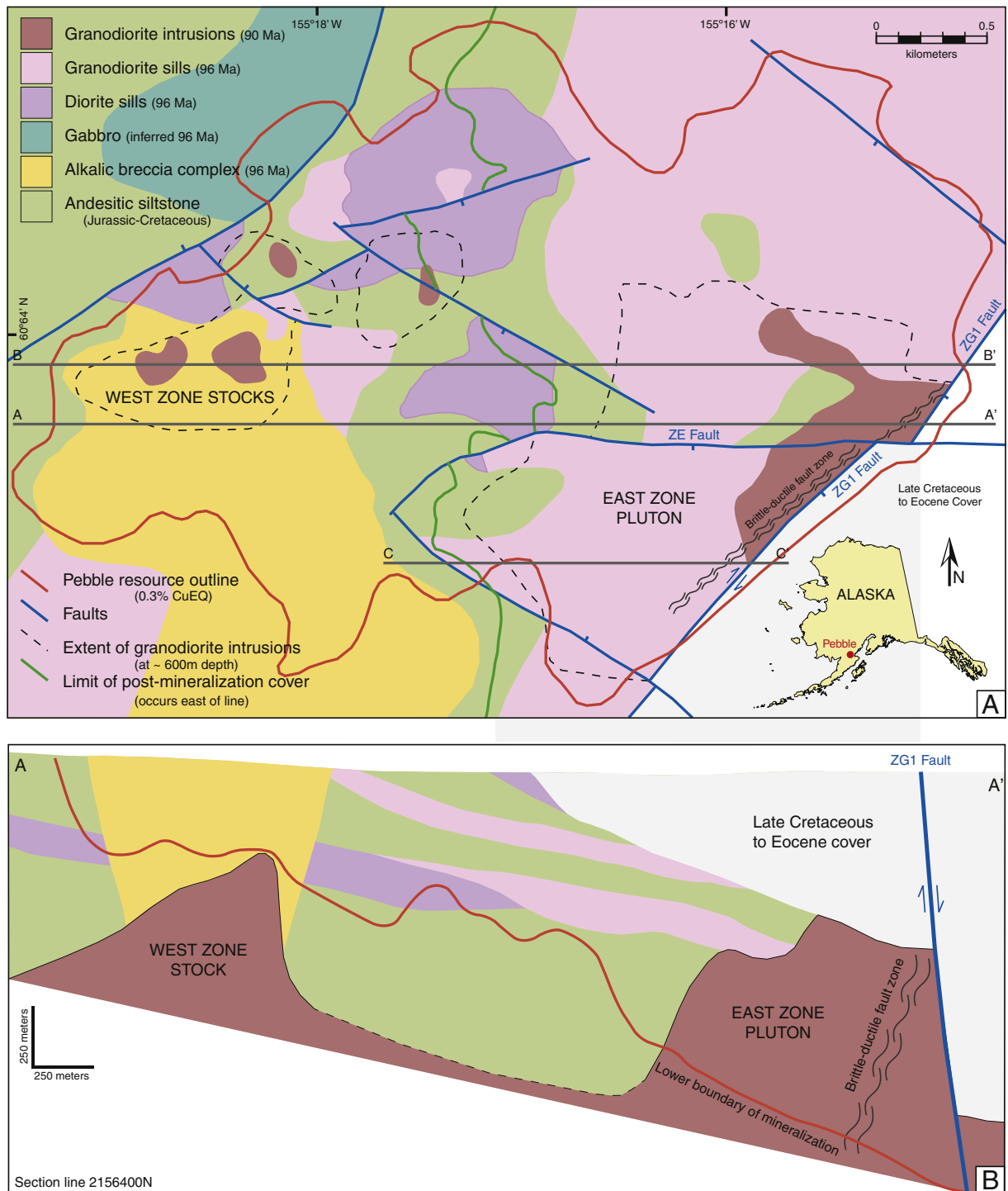
Fig. 1. Geology of the Pebble porphyry Cu-Au-Mo deposit. A. Simplified Cretaceous geology map of the deposit area based on drilling. Glacial deposits and post-mineralization rocks units have been removed. B. Geological cross section along line A–A'. CuEQ expresses the combined copper, gold and molybdenum grade as a copper grade based on the dollar value of all the metals (Cu - US$1.85/lb., Au - US$902/oz., Mo - US$12.50/lb.; Pebble Limited Partnership, 2010).

metals. The deposit contains 36.6 million tonnes of copper, 3341 tonnes of gold and 2.5 million tonnes of molybdenum (Pebble Limited Partnership, 2010). Its gold endowment alone is among the largest of all deposits on earth (Sebag, 2012). The deposit is genetically related to ca. 90 Ma granodiorite intrusions and mineralization is hosted by diverse types of hydrothermal alteration assemblages that include sodic-potassic, potassic, illite ± kaolinite, quartz-illite-pyrite, quartz-sericite-pyrite, and advanced argillic assemblages (Lang and Gregory, 2012; Gregory et al., 2013; Lang et al., 2013).

This study uses fluid inclusion and stable isotope data to unravel the fluid history of the Pebble deposit. A particular focus of the study is the relationship of advanced argillic alteration, which is associated with the highest grades of copper and gold in the deposit, to other alteration types and their fluid sources. There is an increasing recognition that advanced argillic alteration and associated mineralization occur in the deeper parts of porphyry deposits (e.g., Oyu Tolgoi, Khashgerel et al., 2009) in addition to longer-recognized occurrences in the epithermal or lithocap environment (e.g., Hedenquist et al., 1998). Advanced

argillic overprints on earlier alteration types commonly augments grade, with corresponding benefits to project economics (e.g., Winant, 2010), and can be an important target for exploration. Understanding the relationship between deep advanced argillic alteration assemblages and the larger but typically lower grade bulk of the mineralization hosted by potassic and other higher temperature assemblages is critical to exploration success.

2. Geology of the Pebble deposit

2.1. Regional geological setting

The Pebble porphyry Cu-Au-Mo deposit occurs within the collapsed Kahiltna foreland flysch basin which accumulated clastic sedimentary and mafic volcanic rocks during the Jurassic and Cretaceous. The Kahiltna basin was bounded to the north by pericratonic and previously amalgamated allochthonous terranes along the continental margin of North America and to the south by the active Talkeetna oceanic arc within the Peninsular-Alexander-Wrangellia (PAW) superterrane (Goldfarb et al., 2013). The Kahiltna basin was folded, complexly faulted and subjected to low-grade regional metamorphism as the PAW superterrane accreted to North America by the late Early Cretaceous (Detterman and Reed, 1980; Hampton et al., 2010). Subsequent to accretion, arc magmatism migrated inland from the waning Talkeetna arc and regional deformation was accommodated by dextral strike-slip faults parallel to the continental margin (Goldfarb et al., 2013). Mid-Cretaceous magmatism that is spatially, and in part genetically, related to formation of porphyry hydrothermal systems in the Pebble area is interpreted to represent melting of metasomatized subcontinental lithospheric mantle during subduction of oceanic crust below the continental margin (Goldfarb et al., 2013). The main trace of the Lake Clark dextral strike-slip fault zone is located a few kilometers southeast of the Pebble deposit (Anderson et al., 2013) and subsidiary structures related to it may have influenced the emplacement of Cretaceous intrusions in the vicinity of the deposit (Lang et al., 2013).

2.2. Rock types and structures

The Pebble porphyry Cu-Au-Mo deposit formed within a very large magmatic-hydrothermal system related to hornblende granodiorite intrusions emplaced at 91–89 Ma (Fig. 1; Bouley et al., 1995; Lang and Gregory, 2012; Lang et al., 2013; Olson et al., 2013). Host rocks to these intrusions include siltstones and minor wackes of the Kahiltna flysch, several sub-parallel diorite and granodiorite sills which intruded the flysch at ~96 Ma, and a group of slightly younger porphyritic monzonite to monzodiorite intrusions of alkalic composition, along with spatially and temporally related intrusion breccias, which also formed at ~96 Ma (Fig. 1B). The largest body of hornblende granodiorite in the vicinity of Pebble is the Kaskanak batholith, a multiphase intrusion exposed west of the deposit but which is also interpreted from magnetic, electromagnetic and magnetotelluric surveys to extend eastward beneath the deposit (Shah et al., 2009; Anderson et al., 2013). Mineralization at Pebble is centered on and contemporaneous with porphyritic hornblende granodiorite intrusions which occur as several small plugs in the western part of the deposit and the larger East Zone pluton in the east (Fig. 1). Deep drilling indicates that below 1000 to 1500 m depth the porphyritic intrusions are hosted by an equigranular, coarser-grained hornblende granodiorite comparable to the most common phase of the Kaskanak batholith. The Pebble deposit was uplifted and partially eroded sometime during the Late Cretaceous and was subsequently reburied by a post-hydrothermal cover sequence of interbedded clastic sedimentary and volcaniclastic rocks. The deposit was again subjected to erosion in the late Miocene, based on Ar-Ar isotopic dates of 6 Ma and 8 Ma on supergene jarosite reported by Kelley et al. (2011). This erosion occurred after the deposit was tilted approximately 20 degrees to the east sometime during the Paleogene; as a consequence the western part of the deposit was exposed, whereas the eastern part of the deposit remained concealed by an eastward-thickening wedge of cover sequence strata (Fig. 1B). The deposit and cover sequence are now, with the sole exception of one small outcrop in the west, entirely concealed by unconsolidated Pleistocene glacial sediments a few to tens of meters in thickness.

Mineralization at Pebble has been dated at ~89.7 Ma by five Re-Os ages on molybdenite (Lang et al., 2013). Higher grade mineralization occurs within and surrounding the East Zone pluton, whereas mineralization of more moderate grade is spatially associated with the smaller porphyritic granodiorite plugs to the west. Higher grade mineralization in the eastern part of the Pebble deposit was, at least in part, controlled by a northeast-trending structural zone characterized by distributed brittle-ductile deformation (Fig. 1; Lang et al., 2013). This fault was active before, during and after both magmatic and hydrothermal activity related to Pebble and is interpreted to have been an important conduit for mineralizing fluids throughout the hydrothermal history of the deposit (Lang et al., 2013). Brittle-ductile deformation does not extend into the cover sequence. The fault has dextral-oblique displacement with a maximum of 400 m of lateral displacement and an undetermined amount of vertical displacement (S. Goodman, pers. comm., 2008). The deposit is also cut by numerous brittle faults. The most important of these is the northeast-striking, steeply east-dipping ZG1 fault. The ZG1 fault has 650 to 900 m of normal displacement and forms the eastern margin of the deposit (Fig. 1; Lang et al., 2013). The ZE brittle fault is east-striking and steeply south-dipping, cuts through the center of the deposit and has up to 300 m of normal displacement such that mineralization to its north represents a relatively deeper hydrothermal paleodepth compared to the south (Lang et al., 2013). Other brittle faults with constraints on their movement typically exhibit a few tens to perhaps 100 m of mostly normal displacement. The absolute timing of brittle faulting is not well-constrained.

2.3. Hydrothermal alteration and veins

Hydrothermal alteration at Pebble is divided into six major types (Table 1). These have been delineated by logging of drill core, short-wave infrared spectral analysis (Harraden et al., 2013), geochemistry, optical petrography, and SEM-based mineral mapping (Lang and Gregory, 2012; Gregory et al., 2013; Lang et al., 2013; Mathur et al., 2013). Hydrothermal alteration and mineralization are interpreted to have formed during two principal stages (Gregory et al., 2013; Lang et al., 2013). The first stage contains Cu-Au-Mo mineralization which precipitated during sodic-potassic and potassic alteration. During the second stage, additional Cu-Au mineralization was introduced during formation of sericite- and pyrophyllite-bearing subtypes of advanced argillic alteration. An intervening stage of low temperature illite ± kaolinite alteration, which did not introduce additional ore metals, indicates that there was a sufficient gap in time between the two mineralizing stages for the system to cool substantially. Quartz-sericite-pyrite (QSP) alteration forms a wide halo to the deposit and overprints other alteration types; a zone of quartz-illite-pyrite alteration remains in the upper-center of the deposit and may represent the relict of a QSP cap modified by a younger illite overprint. Among these alteration types, illite and sericite have been differentiated using short-wave infrared, x-ray diffraction and illite crystallinity studies (Harraden et al., 2013). This study found that all fine-grained white mica in the deposit was compositionally illite but the more crystalline variety referred to locally as sericite has a composition closer to muscovite. The terms illite and sericite are used to clearly distinguish the two varieties that have different geological settings. The following summaries of the hydrothermal alteration assemblages and vein types at Pebble are based on the detailed descriptions presented in Lang and Gregory (2012), Gregory et al. (2013), and Lang et al. (2013).

Table 1
Hydrothermal Alteration in the Pebble Deposit.

Hydrothermal alteration	Cu (wt%)	Au (ppm)	Mo (ppm)	Ag (ppm)	Mineralogy	Distribution	Timing
Sodic-potassic	0.27	0.29	199	1.36	Albite, K-feldspar, quartz, biotite, magnetite, ankerite, chlorite, calcite, epidote, hematite, pyrite, chalcopyrite, molybdenite	Western half of deposit and at depth below the potassic alteration zone.	Pre- to early syn-potassic alteration.
Potassic	0.55	0.36	280	1.88	K-feldspar, quartz, biotite, chalcopyrite, pyrite, molybdenite, ± bornite	Eastern half of the deposit.	Syn- to post-sodic-potassic alteration.
Quartz-sericite-pyrite	0.20	0.22	78	1.28	Quartz, sericite, pyrite	Forms halo around the deposit, peripheral to sodic-potassic and potassic alteration.	Overprints and pervasively replaces sodic-potassic and potassic alteration around periphery of the deposit.
Illite ± kaolinite	NA	NA	NA	NA	Illite, pyrite, ± kaolinite	Variable intensity overprint found throughout the deposit.	Overprint on sodic-potassic, potassic and some parts of the quartz-sericite-pyrite alteration, older alteration mineral assemblages mostly preserved.
Quartz-illite-pyrite	0.27	0.37	102	1.98	Quartz, illite, K-feldspar, pyrite	Center of deposit at shallow depth.	Composite alteration zone with partially preserved potassic and sodic-potassic alteration that has been overprinted first by weak quartz-sericite-pyrite alteration and then by strong illite alteration where sercite is replaced by illite.
Advanced argillic	0.84	0.56	317	2.69	Quartz, sericite, pyrophyllite, chalcopyrite, pyrite, molybdenite, bornite, digenite, ± enargite	Structurally controlled zone located on the eastern side of the deposit.	Overprints and pervasively replaces potassic and illite ± kaolinite alteration types.

Note: Average grades based on average of all assay intervals that fall within the alteration zone.

2.3.1. Major alteration types

Sodic-potassic and potassic alteration are the earliest alteration types preserved in the Pebble deposit (Table 1). Potassic alteration is concentrated near the top of the East Zone pluton and its host rocks, whereas sodic-potassic alteration occurs below potassic alteration in the east and is the main assemblage in the western half of the deposit (Fig. 2). A volumetrically limited, magnetite-rich subtype of sodic-potassic alteration occurs only within and proximal to diorite sills in the western part of the deposit. Both alteration types contain K-feldspar, quartz and biotite; sodic-potassic alteration is distinguished primarily by a much higher concentration of carbonate minerals and the presence of albite and minor magnetite. Disseminated mineralization spatially associated with potassic and sodic-potassic alteration occurs as chalcopyrite, molybdenite and pyrite, and bornite is a minor but widespread phase in the potassic alteration zone. The grade of copper, molybdenum and gold is, on average, higher in the potassic alteration zone than in the sodic-potassic alteration zone (Table 1). The sodic-potassic alteration which underlies potassic alteration in the east also contains epidote, calcite, chlorite and hematite. The intensity of sodic-potassic alteration and both grade and the concentration of sulfide minerals becomes gradually weaker with depth. Sodic-potassic alteration is interpreted to be slightly pre- to syn-potassic alteration and the common observation that potassic alteration replaces sodic-potassic alteration near their contacts reflects telescoping during cooling (Lang et al., 2013).

Quartz-sericite-pyrite (QSP) alteration forms a wide halo that extends 4 km south and to the limits of drilling 1.5 km to the north of the mineral resource (Lang and Gregory, 2012). This alteration assemblage completely overprints and replaces sodic-potassic and potassic alteration and sulfide mineralization around the periphery of the deposit, with a transitional zone of partial replacement tens to 200 m in width. The QSP alteration almost completely removes pre-existing copper and molybdenum mineralization but it retains highly anomalous concentrations of gold (Gregory et al., 2013). In the approximate center of the deposit is a relict zone of what is interpreted to have been a QSP cap to the deposit which has partially replaced early sodic-potassic and potassic alteration and associated mineralization (Fig. 2) but has, in turn, been overprinted by illite (see below). Although it is likely that this illite-bearing alteration initially formed as typical QSP alteration, it is treated separately as quartz-illite-pyrite alteration because it forms an important metallurgical domain at Pebble (Gregory et al., 2013).

Low temperature, selectively-pervasive illite and illite-kaolinite alteration overprinted most of the Pebble deposit as the early hydrothermal system cooled. Illite is present throughout the deposit and typically replaces hydrothermal K-feldspar, whereas kaolinite is mostly found in the western part of the deposit where it more typically replaces hydrothermal albite. Biotite is variably, but typically more weakly, replaced by illite. The intensity of this low temperature overprint varies from incipient to very strong and the affected volume broadly coincides with the distribution of potassic and sodic-potassic alteration. Dilatant veins are not associated with this alteration but fractures lined by illite and/or kaolinite are common.

Advanced argillic alteration is spatially related to the zone of brittle-ductile faulting on the eastern margin of the deposit and is mostly preserved in the downthrown block south of the ZE normal fault (Fig. 2). This alteration has an overall mineral association of quartz-sericite-pyrophyllite-pyrite-chalcopyrite-bornite-digenite, which is consistent with advanced argillic alteration as described by Meyer and Hemley (1967). Rock affected by this alteration has the highest grades of copper and gold in the Pebble deposit (Table 1). Advanced argillic alteration replaces early potassic and intermediate stage illite alteration. This alteration contains the pyrophyllite and sericite subzones, which collectively form the advanced argillic alteration type due to their contemporaneous, zonal relationship (Lang et al., 2013). The inner pyrophyllite subzone is largely spatially coincident with, and overprints, the zone of brittle-ductile deformation textures and is characterized by quartz-pyrophyllite-sericite alteration accompanied by high concentrations of disseminated chalcopyrite and pyrite. In the outer sericite subzone, quartz-sericite selectively replaced illite-altered hydrothermal feldspar, and was accompanied by chalcopyrite and tennantite; where sericite alteration is most intense, pre-existing alteration was completely replaced and the earlier chalcopyrite and pyrite were commonly replaced along their rims by a high-sulfidation assemblage of pyrite-bornite-digenite ± enargite ± covellite. Where the two minerals coexist, pyrophyllite replaces sericite.

2.3.2. Veins

Ten different vein types are documented in the Pebble deposit (Table 2; Lang and Gregory, 2012; Lang et al., 2013) and are the source of fluid inclusion data reported herein. Vein types EB, A, B, M and C are found throughout the sodic-potassic and potassic alteration zones. All
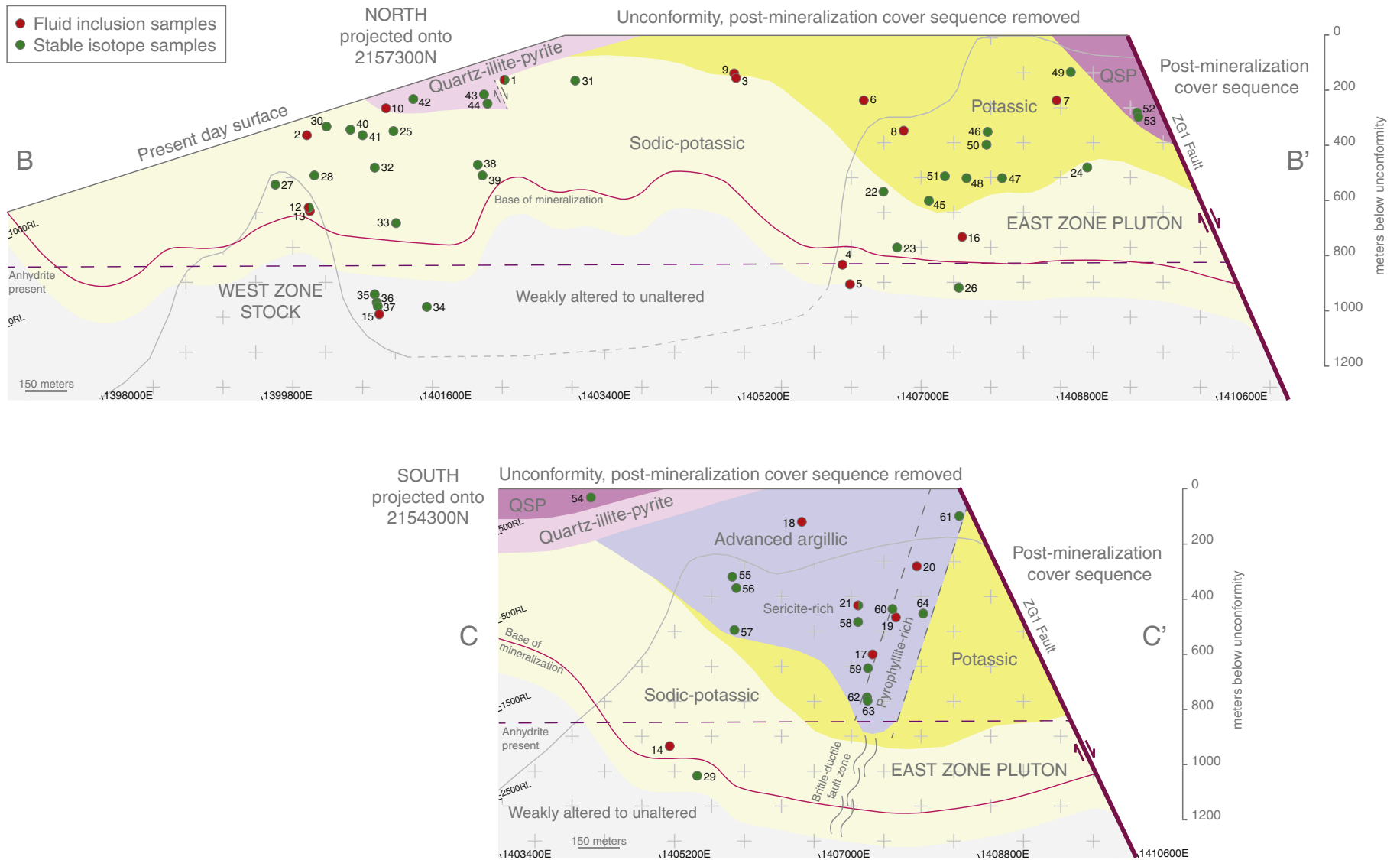
Fig. 2. Location of fluid inclusion and stable isotope samples projected on to representative alteration cross sections to the north and south of the ZE fault (cross section locations shown on Fig. 1). Cross sections have been rotated to reflect orientation at time of mineralization and younger cover rocks have been removed. Due to the offset across the ZE fault, the unconformity occurs at different present day depths to the north and south. Numbers next to each sample location correspond to numbers in Tables 3 and A1. Low temperature illite ± kaolinite alteration occurs as an overprint with variable intensity throughout the sodic-potassic, potassic, quartz-illite-pyrite and quartz-sericite-pyrite zones and is not shown as a spatially defined alteration zone. QSP - quartz-sericite-pyrite. Base of mineralization defined by 0.3 CuEQ cutoff (see Fig. 1 for definition of CuEQ).

these vein types have vein and envelope mineralogy that is the same as the mineralogy which makes up the pervasive alteration of the vein host rock, i.e., quartz, biotite, K-feldspar and/or albite.

Type EB (early biotite) veins may be the oldest in the deposit, although their timing is not fully constrained, and they may be similar to the EB veins of Gustafson and Quiroga (1995). They are biotite-rich, contain low to moderate concentrations of pyrite and chalcopyrite, and have narrow alteration envelopes which contain biotite and K-feldspar. They occur predominantly as narrow fractures in the Kahiltna flysch. Type EB veins did not host usable fluid inclusions but were utilized for light stable isotope analysis.

Type A veins are most common in the granodiorite stock on the east side of the deposit. The type A vein group contains three subtypes at Pebble (Lang et al., 2013) but this study only utilized the most common and widespread Type A1 and A2 veins. Type A1 veins are discontinuous and have diffuse contacts with their host rocks. They are dominated by clear quartz (e.g., Fig. 3A), commonly accompanied by minor K-feldspar. Sulfides range from absent to concentrations of two volume percent and, where present, include trace to minor pyrite, chalcopyrite and/or molybdenite. Narrow alteration envelopes which contain K-feldspar are common. Type A1 veins are similar to the A veins of Gustafson and Hunt (1975). Type A2 veins are transitional between quartz veins and pegmatite and occur at depths below 1000 m within the East Zone pluton. These veins have selvages of K-feldspar and cores of coarse-grained quartz, contain clots of brown biotite, and trace chalcopyrite, molybdenite and/or pyrite (e.g., Fig. 3B). Alteration envelopes are absent. Type A1 and A2 veins are interpreted to be the earliest quartz veins in the deposit and predate the majority of mineralized veins. Type A2 vein textures suggest fluid exsolution occurred directly from a magma.

Type B1 veins occur throughout the deposit and are most common within, and in decreasing density with distance from, the East Zone pluton. Similar patterns are evident within and surrounding the smaller granodiorite intrusions in the western part of the deposit, although the overall vein density is lower. Type B1 veins at Pebble are generally similar to the B veins of Gustafson and Hunt (1975). Type B1 veins are planar, continuous, have sharp contacts with host rocks and vary widely in thickness. Distinct alteration envelopes of highly variable width contain biotite as the main mineral in more iron-rich host rocks, such as the Kahiltna flysch, whereas K-feldspar is relatively more abundant in more felsic host rocks. Vein fill is mostly clear quartz accompanied by trace to minor biotite, K-feldspar, apatite and/or rutile. Sulfide concentration is typically two to five volume percent (e.g., Fig. 3C) but can be locally higher (e.g., Fig. 3D) and consists of subequal pyrite and chalcopyrite with minor molybdenite and, locally, minor bornite. Anhydrite-bearing Type B1 veins (Fig. 3E) are rare and have only been encountered at depths greater than ~730 m below the contact with the overlying cover sequence and its westward projection. Type B1 veins overprint Type A1 veins and make the largest contribution to the overall grade of the deposit due to their large number compared with other vein types. Type B2 veins are temporally equivalent to type B1 but occur mostly at depth in the East Zone. They are distinguished from type B1 veins by weaker alteration envelopes, lower sulfide concentration, green chlorite pseudomorphs after coarse aggregates of brown biotite and minor to rare calcite and epidote.

In the eastern part of the deposit, the density of Type B1 veins and, to a lesser extent, Type A1 veins grades from background values of approximately 5 to 10 vol% into two zones which contain over 80 vol% vein quartz. One zone is coincident with brittle-ductile deformation within the East Zone pluton south of the ZE fault, whereas the other occurs within the East Zone pluton just north of the ZE fault. These zones are interpreted to represent long-lived conduits of high fluid flux that controlled fluids related to both early sodic-potassic and potassic alteration and later advanced argillic alteration (Lang and Gregory, 2012; Lang et al., 2013).

Type B3 veins are younger than Type B1 veins and some even cross cut Type C veins (see below). They are distinguished by a high concentration of molybdenite (e.g., Fig. 3F), which ranges from coarse selvages

within quartz veins to massive infill of dilatant fractures. Other sulfide minerals are rare. Alteration envelopes are weak to sporadic and contain K-feldspar. These veins are most common in the deeper parts of the central and eastern parts of the deposit and extend to the limits of drilling at ~1800 m depth. Where abundant, these veins significantly augment molybdenum grade.

Type C veins are very common in the western half of the deposit but are rare elsewhere. Type C veins at Pebble are locally defined and do not resemble the C veins of Gustafson and Quiroga (1995). They are planar, have sharp contacts with host rock and are highly variable in width. These veins contain quartz, locally abundant ankerite, and minor to trace K-feldspar, magnetite and biotite. In contrast to earlier vein types, they commonly contain up to 50 vol% subequal pyrite and chalcopyrite and, locally, trace to minor bornite and arsenopyrite. Type C veins have wide, very well mineralized alteration envelopes mineralogically similar to the vein fill; locally these envelopes coalesce and return copper grades of several percent. Type C veins cross cut Type B1 veins.

Type M veins typically contain 25 to 75 vol% magnetite and occur only within and proximal to iron-rich diorite sills in the western part of the deposit. They also contain quartz, ankerite and minor K-feldspar and typically include >10 vol% combined pyrite and chalcopyrite (Fig. 3G). Ubiquitous, narrow alteration envelopes contain K-feldspar, quartz, magnetite, pyrite and chalcopyrite. Type M veins at Pebble are similar to M veins as defined by Clark (1993). Paragenetically Type M veins formed after Type B1 veins; they overlap in time with Type C veins, of which they may be a variant.

Veins directly associated with the advanced argillic alteration are denoted Type AA and have a low overall density. Within the pyrophyllite alteration subtype they occur as irregular forms that are mostly <1 cm in width and which contain high concentrations of pyrite and chalcopyrite with minor quartz. These veins commonly overprint or reopen pre-existing quartz veins (e.g., Fig. 3H). Veins directly related to the sericite alteration subtype are also uncommon; they are narrow, commonly irregular in form (e.g., Fig. 3I), contain mostly quartz-pyrite and have distinct sericite alteration envelopes that at least locally contain high-sulfidation copper minerals (Lang et al., 2013).

Both QSP and quartz-illite-pyrite alterations are directly related to type D veins (Table 2: Gustafson and Hunt, 1975). Type D veins are dominated by pyrite and quartz and are enclosed in wide, intense alteration envelopes that contain mostly quartz, pyrite and sericite. The alteration envelopes coalesce to form intense, pervasive QSP alteration where vein density is high.

2.3.3. Metal distribution

Variations in copper, gold and molybdenum grades display a spatial relationship with both rock type and alteration assemblage (Gregory et al., 2013; Lang et al., 2013). All three metals are associated with a chalcopyrite-pyrite-molybdenite assemblage that occurs as both disseminations and in veins. Copper and gold grades are highest in the advanced argillic and potassic alteration zones, moderate grades are characteristic of the sodic-potassic alteration zone and low grades are found in the QSP and quartz-illite-pyrite zones (Table 1; Gregory et al., 2013). Bornite is a minor phase that occurs intergrown with chalcopyrite in the potassic and sodic-potassic alteration zones and as a bornite-digenite-pyrite assemblage in the sericite-rich part of the advanced argillic alteration zone. Molybdenum is the only metal that exhibits a strong spatial relationship with rock type, with higher grades concentrated in deeper parts of the East Zone pluton and its immediate country rocks where type B3 veins are more common (Gregory et al., 2013; Lang et al., 2013). Therefore, molybdenum is at least partially decoupled from copper and gold concentrations.

The majority of gold occurs as inclusions in chalcopyrite and pyrite (90%) with the remainder occurring as inclusions in non-sulfide minerals, dominantly quartz, K-feldspar and carbonate (Gregory et al., 2013). Gold inclusions, accompanied by chalcopyrite and pyrite inclusions, have been identified enclosed by single K-
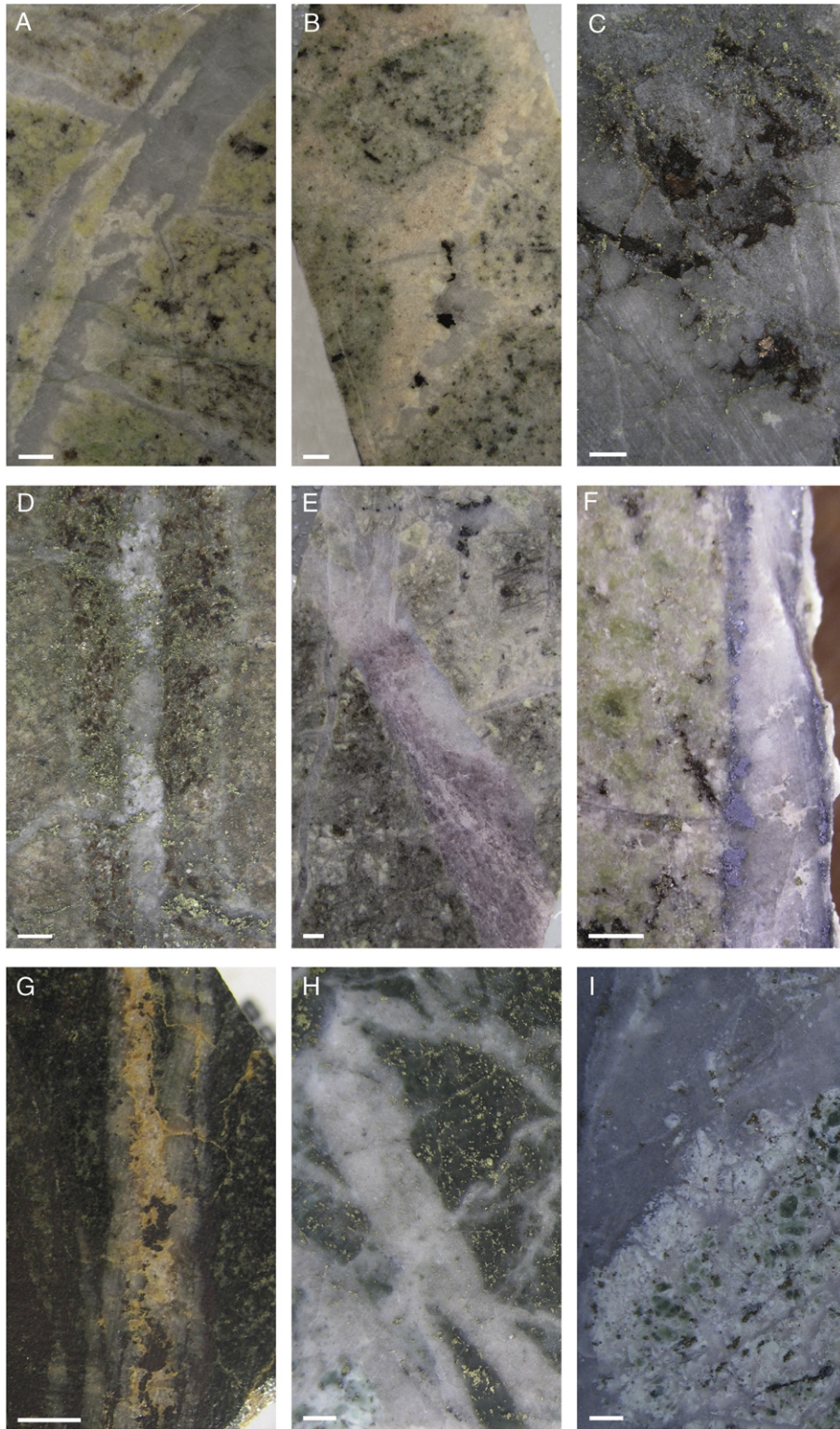
Fig. 3. Examples of vein types in the Pebble deposit and samples used for fluid inclusion analysis. A. A1 vein, quartz vein with feldspar envelope, sample 7363-4008, weak sodic-potassic alteration. B. A2 vein, quartz-feldspar-biotite pegmatite vein, sample 7363-3766, weak sodic-potassic alteration. C. B1 vein, quartz-biotite-pyrite-chalcopyrite vein, sample 7381-2636, potassic alteration. D. B1 vein, quartz-chalcopyrite-pyrite vein with biotite envelope, sample 8440M-1173, potassic alteration. E. B1 vein, quartz-anhydrite vein, sample 11529-2480.9, weak sodic-potassic alteration. F. B3 vein, quartz-molybdenite vein with calcite infill, sample 7392M-1123, weak sodic-potassic alteration. G. M vein, quartz-magnetite-ankerite vein, sample 7399M-286, sodic-potassic alteration. H. AA vein, quartz(-chalcopyrite-pyrite) vein, sample 8422-2919, pyrophyllite alteration. I. AA vein, quartz(-pyrite-chalcopyrite) vein, sample 7360-1590, sericite alteration. Scale bar is 5 mm.

feldspar crystals suggesting K-feldspar and metals were precipitating at the same time (Fig. 4). This is most common in the potassic alteration zone but was also found in some sodic-potassic zone samples.

3. Fluid inclusion study

Fluid inclusions were studied petrographically and with microthermometry with two main objectives: (1) to constrain the

Table 2
Vein types in the Pebble Deposit.

Vein	Vein mineralogy	Vein envelope	Distribution	Timing	Geometry	Association with mineralization
EB	Biotite, (pyrite, chalcopyrite)	Narrow biotite and/or K-feldspar	Concentrated in sedimentary rocks	Pre-dates all other vein types	Narrow fracture fill	Pre-mineralization
A1	Quartz, K-feldspar, (pyrite, chalcopyrite, molybdenite)	Where present narrow K-feldspar	Concentrated in the eastern half of the deposit.	Earliest veins associated with the hydrothermal system	Sinuous, discontinuous, diffuse contacts with host rocks	Earliest veins that host sulfide mineralization
A2	Quartz, K-feldspar, (biotite, pyrite, chalcopyrite, molybdenite)	Absent	Only found deep in the East Zone pluton	Earliest veins associated with the hydrothermal system	Same as for A1 veins	Earliest veins that host sulfide mineralization
B1	Quartz, chalcopyrite, pyrite, molybdenite, (bornite, biotite, K-feldspar, apatite, rutile, anhydrite)	Where present mineralized K-feldspar or biotite	Throughout the deposit but most abundant in the east	Overprint A1 veins	Planar, continuous, sharp contacts with host rocks	Host the majority of sulfide mineralization in the deposit
B2	Quartz, chlorite, pyrite, (chalcopyrite, molybdenite, calcite, epidote)	Weak K-feldspar and/or chlorite	Deep in the eastern part of the deposit	Same timing as B1 veins	Same as for B1 veins	Host minor sulfide mineralization
M	Magnetite, quartz, ankerite, K-feldspar, chalcopyrite, pyrite, (molybdenite)	Narrow envelopes containing K-feldspar, quartz, magnetite, pyrite and/or chalcopyrite	Within and proximal to diorite sills in the western part of the deposit	Overprint B1 veins and overlap in timing with C veins	Planar to irregular	Can host high volumes of sulfide mineralization
C	Quartz, ankerite, chalcopyrite, pyrite, (molybdenite, K-feldspar, magnetite, biotite, bornite, arsenopyrite)	Wide, well mineralized envelopes of K-feldspar or biotite	Throughout the deposit but most common in the west	Overprint B1 veins, contemporaneous with some M veins	Planar, sharp contacts with rock rocks	Typically host high volumes of sulfide mineralization and related to local zones of high grade
B3	Quartz, molybdenite	Weak and sporadic envelopes of K-feldspar	Concentrated in the central and eastern parts of the deposit, particularly at depth	Overprint B1 and some C veins	Same as for B1 veins	Major contributor to molybdenum grade
D	Pyrite, quartz	Wide quartz, sericite/illite, pyrite envelopes	Found within zones of quartz-sericite-pyrite and quartz-illite-pyrite alteration	Overprint all types of A, B, C and M veins	Planar	Do not host mineralization
AA	Quartz, pyrite, chalcopyrite, (bornite, digenite, enargite)	Some with envelopes that contain quartz, sericite, pyrite, chalcopyrite, bornite, digenite, and/or enargite	Found within the advanced argillic alteration zone in the east of the deposit	Reactivates and overprints massive quartz-rich brittle-ductile zone that was most likely originally composed of A1 and B1 veins	Narrow and irregular	Host mineralization related to the advanced argillic alteration event

Note: Vein nomenclature, mineralogy, distribution and timing data from Lang and Gregory (2012) and Lang et al. (2013).

pressure, temperature and salinity of fluids related to quartz vein formation and their associated alteration mineral and metal assemblages; and (2) to obtain temperatures to inform calculation of the isotopic signature of the fluids. The fluid inclusion data from Tracy (2001) will, to the extent possible in light of limited sample documentation and restriction of data to the western part of the deposit, be incorporated into the interpretation for Pebble in later sections of this study.

3.1. Sample selection

The petrographic characteristics of fluid inclusions were examined in over 100 thin sections, from which 20 were chosen for microthermometry. The selected samples represent quartz-rich veins hosted by each of the major alteration types in the deposit (Table 3). The samples come from depths of approximately 30 to 1000 m below the nearly planar unconformity, and its westward projection, with post-hydrothermal rock types (Fig. 2), which has been interpreted as a possible datum approximately parallel to the paleosurface at the time of hydrothermal activity (Lang et al., 2013).

### 3.2. Sample preparation and microthermometry methods

The samples were prepared as doubly polished sections 100 μm in thickness. They were examined using transmitted-light microscopy to select high quality, representative fluid inclusion assemblages for analysis. Cathodoluminescence imaging was used to distinguish different temporal generations of quartz within the veins and their relationship to the

fluid inclusion assemblages. Cathodoluminescence was undertaken on a JEOL™ JSM 6300 scanning electron microscope equipped with a monochromatic CL detector at the University of Ballarat. Microthermometry measurements were obtained with a Linkam THMSG 600 heating-freezing stage at the University of British Columbia. The stage was calibrated using synthetic fluid inclusions; low-temperature measurements (<300 °C) are accurate to within ± 1 °C and high-temperature measurements (>300 °C) within ± 5 °C.

3.3. Estimation of salinity and additional fluid components

Salinity is reported as weight percent NaCl equivalent. Salinity calculations assumed a simple H_2O-NaCl system and used ice-melting temperatures for liquid-vapor and intermediate-density inclusions, and halite dissolution temperatures for simple brine inclusions (Bodnar and Vityk, 1994). For brine inclusions where homogenization was by halite dissolution, salinities may be underestimated by up to 1.3 wt% NaCl equivalent (based on the temperature range found in this study) (Bodnar, 1994). Polyphase brine inclusions which contained sylvite and halite used salt dissolution temperatures and the H_2O-NaCl-KCl system (Sterner et al., 1988). Eutectic temperature during heating runs was used to infer the presence of secondary cations such as calcium, iron and magnesium in the fluids, based on data in Borisenko (1977). Phase transitions in vapor-rich inclusions were not observed during heating and freezing. Opaque and transparent daughter minerals other than halite and sylvite did not change visually during heating and freezing runs.
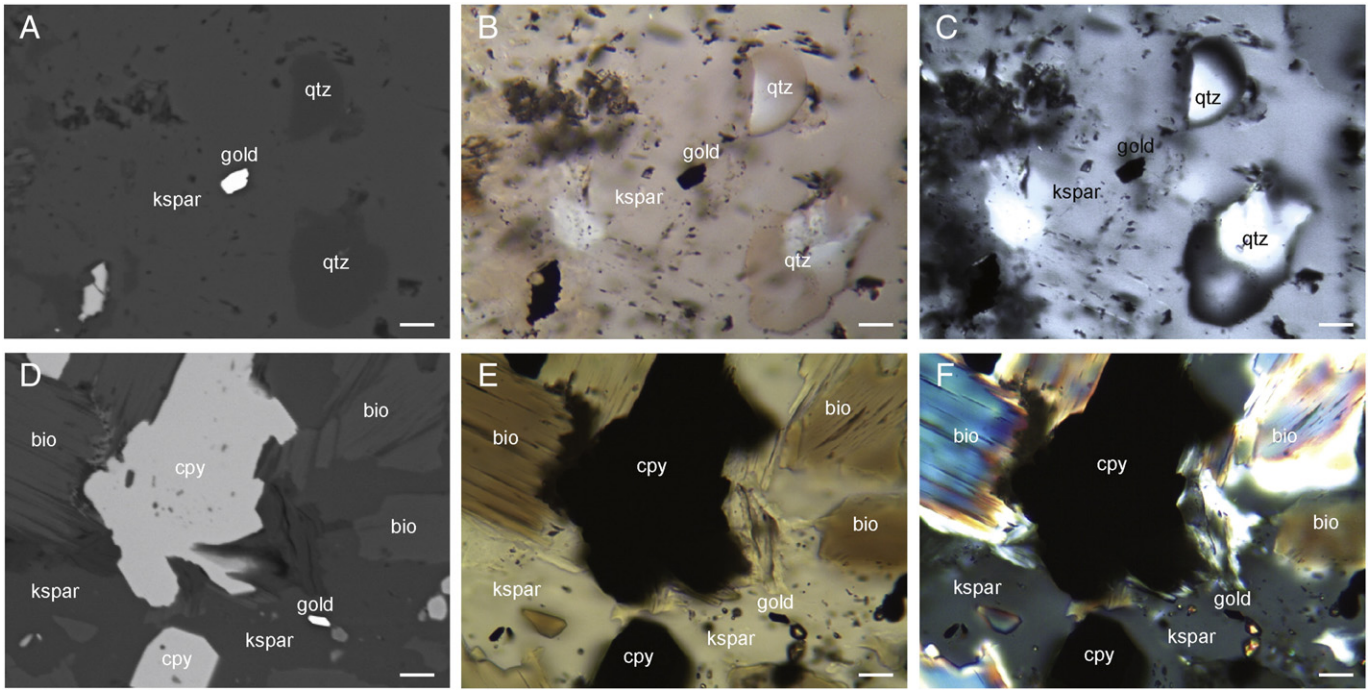
Fig. 4. SEM and petrographic images of gold inclusions in K-feldspar provide evidence for the co-precipitation of potassic alteration minerals and mineralization. Sample 7389-2387: A. SEM image, B. plane polarized light image. C. Cross polarized light image. Sample 8439M-804: E. SEM image, F. plane polarized light image. G. Cross polarized light image. Scale bar is 10 μm. Abbreviations: bio - biotite, kspar - K-feldspar, qtz - quartz, cpy - chalcopyrite.

3.4. Cathodoluminescence characteristics of quartz veins

Cathodoluminescence (CL) imaging of the quartz veins used in this study show three distinct generations of quartz precipitation (Fig. 5). The oldest generation (Q1) is characterized by bright white luminescence in granular quartz that occurs both as large, coherent zones and/or as remnant islands enclosed by younger generations of quartz (Fig. 5A

and C). Second generation quartz (Q2) is characterized by medium CL light intensity in varying shades of grey that typically define oscillatory growth zoning (Fig. 5B). The Q2 quartz encloses, infills around, or forms veinlets which cut, grains of Q1 quartz and is associated with minor sulfide. The youngest generation of quartz (Q3) has a dark grey to black CL response and occurs enclosing sulfide minerals along fractures which cut older quartz generations or which infill areas where older quartz
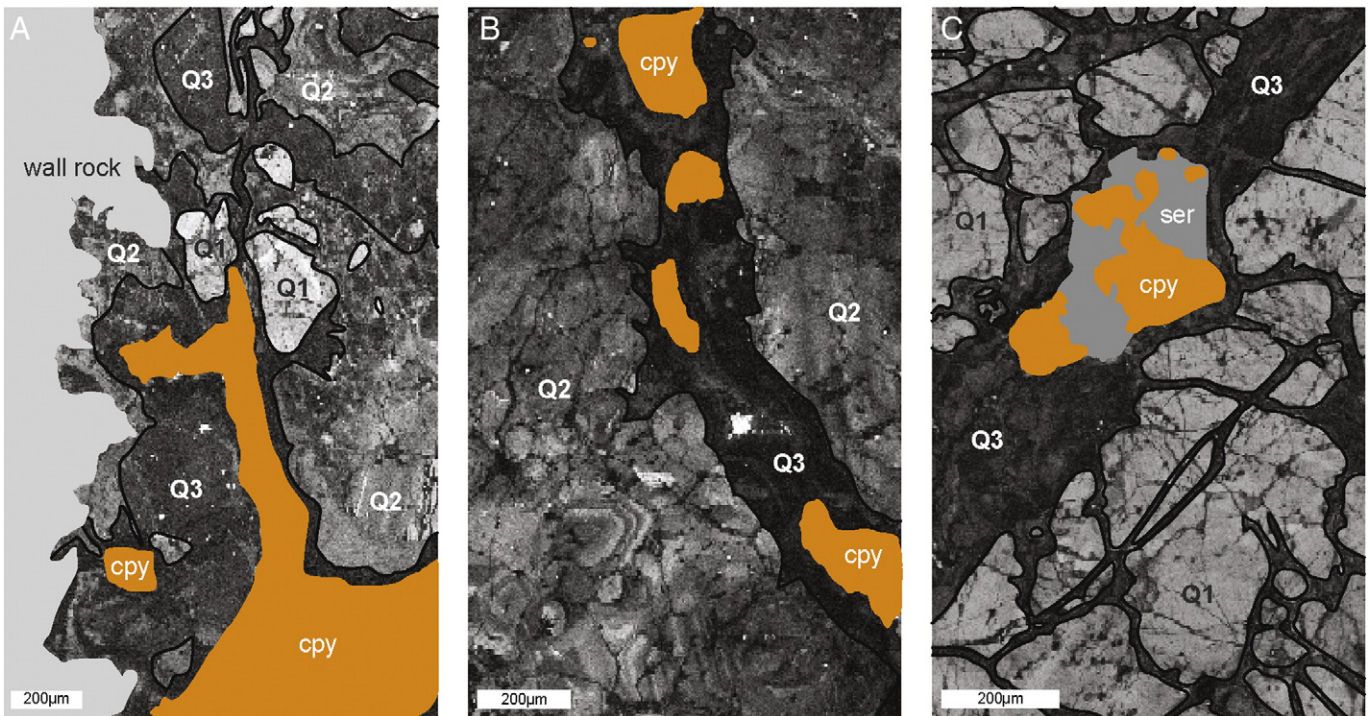
Fig. 5. Cathodoluminescence images of quartz veins. A. Quartz-sulfide B1 vein hosted by potassically altered wall rock. Remnant islands of Q1 quartz enclosed by Q2 quartz are all cut by Q3 quartz which is synchronous with chalcopyrite precipitation. B. Quartz-sulfide B1 vein hosted by potassically altered wall rock. Q3 quartz and chalcopyrite veinlet cuts Q2 quartz. C. Quartz-sericite-chalcopyrite AA vein hosted by sericite altered wall rock. Q1 quartz cut by network of Q3 quartz-sericite-chalcopyrite veinlets. Abbreviations: cpy - chalcopyrite, ser - sericite.

was dissolved (Fig. 5A, B and C). The Q3 quartz is very clear in transmitted light and hosts few fluid inclusions, which contrasts with optically cloudy Q1 and Q2 quartz where fluid inclusions are very abundant.

The major vein types at Pebble host different proportions of the three types of quartz recognized by cathodoluminescence. Type A veins are dominated by Q1 quartz. Type B veins range from those dominated by Q1 quartz with minor Q2 quartz infill between larger Q1 quartz crystals, mainly in veins hosted by sodic-potassic alteration, to those with relicts of Q1 quartz, variable amounts of Q2 quartz (from absent to major) and large volumes of Q3 quartz, mainly in veins hosted by potassic alteration. All three quartz types occur together in veins close to the sodic-potassic to potassic alteration boundary. The Q3 quartz always encloses significant volumes of sulfide minerals. Type AA veins are dominated by older Q1 and Q2 quartz that has been overprinted by minor Q3 quartz that also encloses larger volumes of sulfide minerals, along with sericite and/or pyrophyllite (e.g., Fig. 5C).

3.5. Fluid inclusion microthermometry results

The 20 fluid inclusion samples yielded 94 fluid inclusion assemblages (Table 3), most of which contained 2 to 5 individual fluid inclusions. Five types of fluid inclusions were identified during the study: (1) intermediate-density (50–60% vapor) inclusions (Fig. 6A and B); (2) simple brine inclusions containing liquid-vapor-halite ± daughter phases (Fig. 6C and D); (3) polyphase brine inclusions containing liquid-vapor-halite-sylvite ± daughter phases (Fig. 6E and F); (4) vapor-rich (>90% vapor) inclusions (Fig. 6G); and (5) liquid-vapor (20–40% vapor) inclusions (Fig. 6H). In the section which follows, the codes for fluid inclusion types are constructed to indicate the relative proportions of vapor (V), liquid (L), halite (H) and sylvite (S) present, in order of decreasing abundance. For salt-bearing inclusions, homogenization by disappearance of halite (LVH-H; LVHS-H) or vapor (LVH-V; LVHS-V) is also indicated. Data were obtained from 339 individual fluid inclusions, of which 287 yielded both homogenization temperature and salinity results (Table 3; Fig. 7).

This study concentrated on fluid inclusion assemblages that consist of spatially associated groups of individual, coeval inclusions that are similar in size, shape and phase proportions at room temperature (Goldstein and Reynolds, 1994). The fluid inclusions in the intermediate-density and brine assemblages mostly occur in clusters (Fig. 6I), with fewer cases where they occur along linear inclusion trails that typically do not cross quartz crystal boundaries (Fig. 6J), and are therefore interpreted to be of pseudosecondary or secondary origin. Most liquid-vapor inclusions occur along fractures that cross quartz crystal boundaries, which is consistent with a secondary origin. Individual inclusions are typically subrounded or, less commonly, have negative crystal shapes and range in diameter from 2 to 54 μm with the majority <20 μm. When the fluid inclusion assemblages exhibit internally consistent behavior during freezing and heating they are herein interpreted to represent a single trapped fluid. In the sections which follow, microthermometry results reflect averages for assemblages rather than data from individual inclusions.

3.5.1. Intermediate-density fluid inclusions

Intermediate-density fluid inclusions (VL-ID and LV-ID) occur in A1, A2, B1 and B3 veins that are hosted by sodic-potassic and quartz-illite-pyrite alteration. In the latter case, the veins are related to early sodic-potassic alteration rather than the illite overprint. They are dominantly in Q1 quartz but also occur in Q2 quartz, are most prominent in the deepest samples of A1, A2 and B3 veins, and occur to a lesser extent in shallower B1 veins. These inclusions are most common in samples that also host populations of simple LVH-H brine inclusions that homogenize by halite dissolution at lower temperatures relative to the intermediate-density inclusions. Intermediate-density inclusions are minor in AA veins and rare to absent in B1 veins hosted by potassic alteration. These inclusions commonly contain a triangular opaque daughter mineral interpreted to be chalcopyrite and, less commonly, a tiny transparent mineral. The majority (86%) of the intermediate-density inclusion assemblages homogenize by liquid disappearance (VL-ID inclusions), or rarely by near-critical behavior, between 377 and 506 °C. Final ice melting temperatures in VL-ID inclusions range from −14 to −1 °C corresponding to salinities of 2 to 17 wt% NaCl equivalent with an average of 9.5 wt% NaCl equivalent. Limited eutectic temperatures are near −21 °C and suggest sodium is the dominant cation in the fluid. Liquid CO_2 was not observed in any of the intermediate-density inclusions at room temperature and clathrate was not observed during cooling. Although this indicates that the CO_2 content of the fluid is <2 mol percent (Rosso and Bodnar, 1995), even very low concentrations of CO_2 impact the accuracy of salinity calculations (Bakker, 1997) which are herein considered maxima.

The intermediate-density inclusions that homogenize by vapor disappearance (LV-ID) occur dominantly in Q1 quartz in AA veins and have homogenization temperatures that range from 370 to 498 °C. Large variations between homogenization temperatures within fluid inclusion assemblages suggest these inclusions may have undergone post-entrapment modification and this is consistent with these assemblages being hosted in older quartz that originally formed A1 and B1 veins prior to the advanced argillic overprint. This population of inclusions has ice melting temperatures between −14 and −19 °C corresponding to salinities between 17 and 21 wt% NaCl equivalent, significantly higher than the intermediate-density inclusions that homogenize by liquid disappearance.

3.5.2. Simple brine fluid inclusions

Simple brine inclusions that homogenize by halite dissolution (LVH-H) are hosted by Q1 and Q2 quartz. They are most prominent in A1 and A2 veins and the deepest B1 and B3 veins hosted by weak sodic-potassic alteration. The LVH-H inclusions contain liquid, vapor, halite and a small opaque mineral. LVH-H inclusions are also identified in Q1 and Q2 quartz in AA veins where they typically contain one or two opaque minerals as well as other very small transparent minerals that include a cubic phase with high relief.

Homogenization temperatures for LVH-H assemblages in A1, A2, B1 and B3 veins range from 334 to 439 °C. Salinities range from 41 to 52 wt% NaCl equivalent. Eutectic temperatures are mostly between −44 and −36 °C, which suggests a Mg and/or Fe component in the fluids. The homogenization temperatures and salinities for assemblages hosted by AA veins are 299 to 394 °C and 38 to 48 wt% NaCl equivalent, respectively, which is only slightly lower than in other vein types. The microthermometry results and the CL response of the quartz which hosts the LVH-H assemblages in the AA veins suggests, however, that these inclusions are actually hosted by quartz domains that originally precipitated during formation of older A1 and B1 veins.

Simple brine inclusions that homogenize by vapor disappearance (LVH-V) are hosted by Q1 and Q2 quartz and are confined to B1, M and B3 veins in the sodic-potassic alteration zone. They are rare in AA veins and in veins hosted by potassic alteration. Homogenization temperatures for LVH-V inclusion assemblages range from 281 to 394 °C and salinities range from 35 to 43 wt% NaCl equivalent. The homogenization data separate into lower temperature and higher temperature subgroups.

The higher temperature LVH-V assemblages typically contain a triangular opaque phase interpreted to be chalcopyrite and many contain hematite and one or two transparent minerals, the most common being a large rectangular or rhombic daughter phase with high relief. Homogenization temperatures range from 353 to 394 °C, with salinities that range from 35 to 43 wt% NaCl equivalent. Eutectic temperatures are between −50 and −35 °C, suggesting a Ca or Mg component in the fluids. Intermediate-density inclusions are commonly spatially associated with these brine inclusions and, where this association occurs in B1 veins, they have the same to slightly higher homogenization temperatures, however, it is not clear if these two inclusion types have a genetic relationship. Low-density vapor-rich inclusions also commonly occur as discrete assemblages in the quartz grains which host this brine inclusion population.

Table 3
Average data for measured fluid inclusion assemblages.

| Sample ID[a]	Vein type	Sample description	Vein description	Inclusion type[b]	No[c]	Average length (μm)	Salinity wt% NaCl equivalent			Te	Tm (ice)	Tm (halite)	Tm (sylvite)	Th (V-L)	Th (L-V)	Homogenization temperature °C		
							Min	Max	Ave							Min	Max	Ave
(5) 7363-4008	A1	Weakly sodic-potassic-altered granodiorite pluton	Deep quartz A vein with pink feldspar envelopes	VL-ID	3	11			2		−1				400	396	406	400
				LV	5	8	1	3	2		−1			259		249	266	259
				LVH-H	4	16	39	43	42			342		265		309	385	342
				LV	4	5	2	7	5		−3			314		289	354	314
				LVH-H	5	8	51	52	52			434		266		434	442	439
(4) 7363-3766	A2	Weakly sodic-potassic-altered granodiorite pluton	Coarse-grained quartz-feldspar-biotite pegmatite vein	VL-ID	3	13	10	13	12		−8				506	500	511	506
				LVH-H	4	4	43	45	44			367		308		353	377	367
				VL-ID	6	9	11	18	15		−11				436	375	498	436
				LVH-H	5	7	39	44	41			338		286		312	367	338
				LVH-H	5	11	41	49	46			381		307		336	411	381
				VL-ID	4	11	8	18	14		−10				377	347	420	377
(2) 8424M-357	B1	Sodic-potassic-altered sediment without albite	Quartz-pyrite-chalcopyrite-tennantite	LVHS-H	1	16			58	−49		419	110	404				419
				LVH-V	4	12	42	43	43	−50		351		394		381	408	394
				VL-ID	5	16	3	10	6		−4				387	370	405	387
				VL-ID	5	14	9	14	11	−23	−7				486	443	522	486
				VL-ID	2	16	9	12	10		−7				403	394	412	403
				LVH-H	3	11	42	43	43	−44		352		308		345	356	352
(3) 8440M-1236B	B1	Sodic-potassic-altered sediment	Quartz (-pyrite) with albite envelope	LVH-V	5	9	36	43	39			311		385		362	423	385
				LV	2	5	0	0	0	0				206		206	206	206
				VL-ID	3	17	1	5	3		−2				406	393	417	406
				LVH-V	3	11	41	42	41			337		368		359	386	368
(6) 6338-1992	B1	Potassic-altered sediment	Quartz-chalcopyrite	LV	4	4	2	4	3		−2			254		252	261	254
				LVH-V	2	12	36	36	36	−41		268		364		332	396	364
				LVH-H	4	5	44	47	46			383		222		363	393	383
				LVH-H	4	9	46	48	47			393		369		381	406	395
				LVHS-H	5	15	56	61	59	−48		420	122	313		390	441	420
(7) 7381-2636	B1	Potassic-altered granodiorite pluton	Quartz-biotite-pyrite-chalcopyrite	LVHS-H	4	7			48			302	100	269		285	312	302
				LVHS-V	2	11	50	50	50			326	106	349		341	357	349
				LVHS-H	3	21			49	−49		319	100	291		309	327	319
				LVHS-V	2	17			51			339	106	351		345	356	351
				LV	3	9	1	5	3		−2			327		323	334	327
(8) 7389-2387	B1	Potassic-altered granodiorite sill	Quartz-chalcopyrite-bornite	LVH-H	3	5	44	52	48			406		212		371	443	406
				LV	5	5	2	6	4		−2			272		178	309	272
				LV	5	4	13	23	18		−15			248		221	276	248
(10) 7398M-237	B1	Quartz-illite-pyrite-altered sediment	Quartz-pyrite (-chalcopyrite)	LVH-H	1	10			43	−51		359		330				359
				LVHS-H	1	10			52	−45		363	87	314				363
				VL-ID	3	11	3	10	7		−5				410	401	416	410
				VL-ID	3	6	8	13	11		−8				402	384	424	402
				LV	3	4	14	23	18		−15			298		296	303	298
				VL-ID	3	8	75	16	12		−9				406	396	417	406
				LVH-H	2	7	40	45	43			354		302		328	381	354
(15) 11529-2480.9	B1	Weakly sodic-potassic-altered monzonite	Quartz-anhydrite	LV	4	4	8	11	10		−6			287		257	320	287
				LV	7	5	9	11	10		−7			303		283	316	303
				LVH-V	3	15	38	38	38	−26		297		317		315	321	317
				LV ANH	4	8	4	5	4		−3			168		162	174	168
(16) 8401-3833	B1	Weakly sodic-potassic-altered granodiorite pluton	Quartz-anhydrite-molybdenite vein	LVH-H	6	7	41	48	45	−36		380		272		339	408	380
				LV ANH	3	5	1	5	3		−2			147		128	169	147
				LV ANH	4	6	2	6	4		−2			245		235	258	245
				LV	5	7	5	7	6		−4			288		254	305	288
				LVH-H	8	6	38	44	41			334		253		298	365	334
				LV	4	6	7	11	9		−6			303		300	306	303

Table 3 (*continued*)

Sample ID[a]	Vein type	Sample description	Vein description	Inclusion type[b]	No[c]	Average length (μm)	Salinity wt% NaCl equivalent			Te	Tm (ice)	Tm (halite)	Tm (sylvite)	Th (V-L)	Th (L-V)	Homogenization temperature °C		
							Min	Max	Ave							Min	Max	Ave
(9) 8440M-1173	B1	Potassic-altered granodiorite sill	Quartz-chalcopyrite-pyrite with biotite envelope	LVHS-H	4	13	51	54	53	−52		370	113	261		347	404	370
				LVHS-V	5	18	52	55	54	−48		366	117	375		363	388	375
				LV	2	7	2	3	3		−2			234		231	237	234
				LV-ID	2	7			20	−20	−17				498	462	535	498
(1) 7399M-286	M	Sodic-potassic-altered diorite with strong kaolinite overprint	Quartz-magnetite-ankerite	LV	4	8	3	3	3		−2			337		327	356	337
				LVH-V	4	7	37	38	37	−25		288		301		296	307	301
				LV	3	9	1	3	2		−1			259		235	289	259
(12) 7392M-1107.5	B3	Weakly sodic-potassic-altered granodiorite pluton, igneous plagioclase still present	Quartz vein with molybdenite selvage, minor central calcite infill	LVH-H	2	11	43	43	43	−37		359		333		358	360	359
				LVH-H	5	17	41	41	41	−36		334		323		330	338	334
				VL-ID	2	16			4		−3				395	384	406	395
				VL-ID	3	14			NM						402	394	417	402
(13) 7392M-1123			Quartz vein with molybdenite selvage-central calcite (-chalcopyrite) infill	LV	4	6	6	16	11		−8			291		241	314	291
				VL-ID	3	9	8	22	17		−14				419	411	426	419
				LVH-V	6	9	35	37	36	−38		270		281		278	286	281
				LVH-V	3	11	37	37	37	−36		286		299		293	305	299
				LV	2	8			NM					261		233	288	261
(14) 8418-3888	B3	Sodic-potassic-altered granodiorite pluton	Quartz-molybdenite	VL-ID	3	11	3	14	8		−6				451	410	525	451
				LV	5	5			7		−5			339		319	349	339
				LV	3	6	2	6	4		−2			254		249	258	254
				LV	4	4	4	6	5		−3			316		302	325	316
				LVH-V	5	9	35	37	36	−43		273		353		340	360	353
				LVH-V	5	8	33	37	35	−35		248		353		343	372	353
(17) 11533-3457	AA	Sericite-altered granodiorite pluton	Euhedral quartz with late pyrite (-chalcopyrite) infill	LV	6	6	3	8	5		−3			291		275	300	291
				LV	1	7			3		−2			308				308
				LVHS-H	2	13	48	51	49			333	92	246		326	340	333
				LV-ID	3	10	20	23	21		−19				419	356	482	419
				LVH-V	4	8	37	40	40			318		366		335	396	366
(18) 7360-1590	AA	Sericite-altered granodiorite pluton	Quartz (-pyrite-chalcopyrite)	LVH-H	3	9	40	45	42			342		311		317	371	342
				LV	4	10	1	2	2		−1			312		310	317	312
				LVH-H	3	9	46	50	48			394		300		390	397	394
(19) 7378-3067	AA	Sericite-rich granodiorite pluton in pyrophyllite zone	Quartz (-chalcopyrite-pyrite)	LV	8	7	1	9	4		−2			346		321	382	346
				LVH-H	4	11	35	40	38	−32		299		249		262	319	299
				LV	3	9	1	6	3		−2			323		320	327	323
(20) 8414-2632	AA	Sericite-altered granodiorite pluton in the brittle-ductile deformation zone	Quartz-pyrite (-chalcopyrite) breccia	LVH-H	4	12	43	47	45			378		357		357	393	378
				LV	6	8	0	2	1		−1			356		343	366	356
				LVHS-V	1	18			46	−51		300	69	315				315
				LV-ID	4	7	13	23	17		−14				370	293	491	370
				LVH-H	3	13	37	43	42			346		264		287	392	346
(21) 8422-2919	AA	Pyrophyllite-altered granodiorite pluton	Quartz (-chalcopyrite-pyrite)	LVHS-V	2	19	50	53	52			352	109	439		373	373	373
				VL-ID	2	39	7	12	10	−24	−6				405	396	414	405
				LVHS-H	2	13	50	52	51	−43		348	100	314		338	357	348
				LVH-H	2	16	39	40	39			312		279		305	319	312
				LVH-H	2	14	35	44	40			316		243		260	371	316

[a] Number in parentheses corresponds to numbers on Fig. 2.

[b] Fluid inclusion types (hosted by quartz unless otherwise stated): LV = liquid-vapor, LV ANH = liquid-vapor inclusions hosted by anhydrite, LVH-V = liquid-vapor-halite inclusions where homogenization is by vapor disappearance, LVH-H = liquid-vapor-halite inclusions where homogenization is by halite dissolution, LVHS-V = liquid-vapor-halite-sylvite inclusions where homogenization is by vapor disappearance, LVHS-H = liquid-vapor-halite-sylvite inclusions where homogenization is by halite dissolution, VL-ID = intermediate density inclusions that homogenize by liquid disappearance, LV-ID = intermediate density inclusions that homogenize by vapor disappearance.

[c] No = number of inclusions in assemblage, NM = not measured.
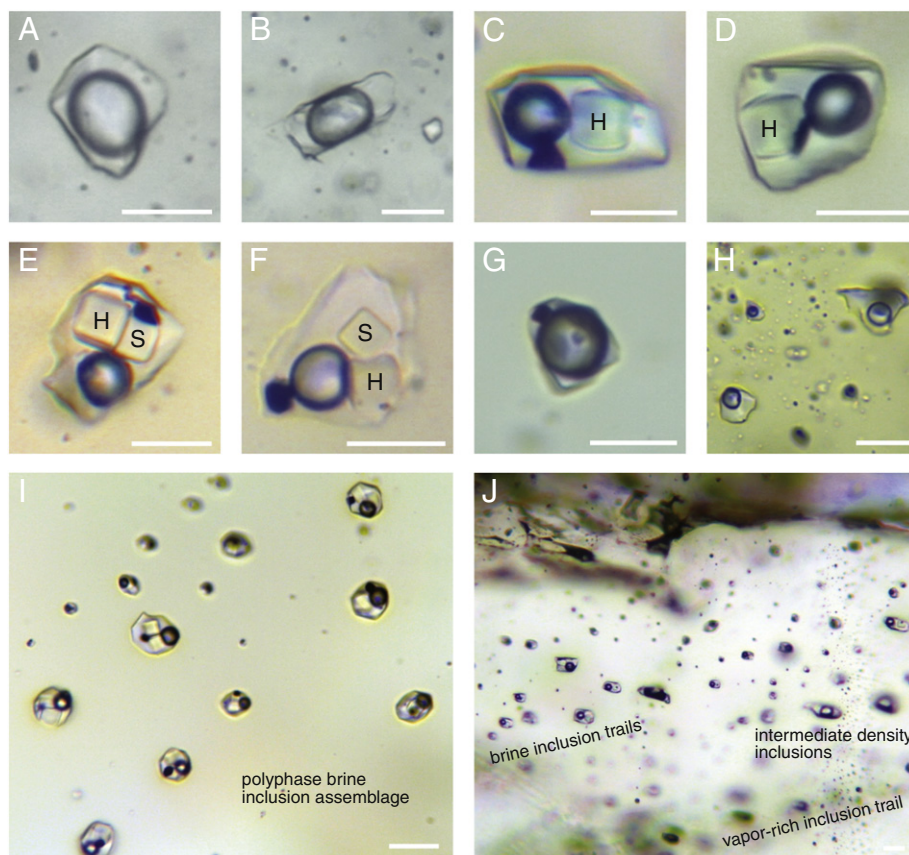
Fig. 6. Examples of fluid inclusions. A-B. Intermediate-density liquid-vapor inclusions. C-D. Liquid-vapor-halite-chalcopyrite inclusions. E–F. Liquid-vapor-halite-sylvite-chalcopyrite inclusions. G. Vapor-rich inclusion. H. Liquid-vapor aqueous inclusions. I. Fluid inclusion assemblage of polyphase liquid-vapor-halite-sylvite brine inclusions. J. Parallel brine inclusion trails and vapor-rich inclusion trails together with associated intermediate-density inclusions. Scale bar is 10 μm, H - halite, S - sylvite.

The lower temperature LVH-V inclusions occur in veins that contain carbonate or anhydrite. These inclusions locally contain an opaque mineral. Homogenization temperatures range from 281 to 317 °C with salinities between 36 and 38 wt% NaCl equivalent. Eutectic temperatures are between −38 and −25 °C, suggesting limited involvement of other cations in the fluids.

The majority of the brine inclusions analyzed by Tracy (2001) were from samples located within the sodic-potassic and quartz-illite-pyrite alteration domains. These liquid-vapor-halite inclusions homogenize by vapor disappearance and are most likely equivalent to the higher temperature population of LVH-V inclusions in this study. Tracy (2001) reported homogenization temperatures between 332 and 518 °C and salinities between 36 and 46 wt% NaCl equivalent, which overlap the data presented in this study.

3.5.3. Polyphase brine fluid inclusions

Polyphase brine inclusions (LVHS-V and LVHS-H) are hosted by Q3 quartz and found dominantly in B1 veins that are associated with potassic alteration. They are a minor inclusion type in AA veins and rare to absent in veins hosted by sodic-potassic alteration. These liquid-vapor-halite-sylvite inclusions contain numerous other daughter minerals that include small clear transparent minerals, some with very high white birefringence (possibly an iron chloride mineral), an orange transparent phase (possibly rutile), hematite and other opaque minerals. The majority of the opaque minerals are triangular in shape and consistent with chalcopyrite. Polyphase brine inclusions homogenize by both vapor disappearance (LVHS-V) and halite dissolution (LVHS-H), with assemblages which exhibit both behaviors commonly found within a given sample. There is no difference in homogenization temperature between the LVHS-V and LVHS-H inclusion types but the LVHS-V inclusions are slightly lower in salinity by an average of 2 wt%

NaCl equivalent. The changing homogenization behavior is due to the high KCl concentration of the fluids (15 to 18 wt% KCl) that is close to the maximum that these fluids can dissolve. Sylvite dissolution temperatures range from 69 to 122 °C and are always lower than halite dissolution temperatures; estimated K/Na ratios range from 0.38 to 0.48 with an average of 0.40. For comparison, simple brine inclusions without sylvite have a K/Na ratio of <0.2 (Roedder, 1984). Polyphase brine inclusions have a range in homogenization temperature from 302 to 420 °C; salinities are between 46 and 59 wt% NaCl equivalent. Eutectic temperatures are tightly clustered between −52 and −48 °C which suggests that the fluids include a $CaCl_2$ component.

3.5.4. Liquid-vapor fluid inclusions

Liquid-vapor inclusions occur in all samples in this study. In A1, B1, M and B3 veins, but not in AA veins, liquid-vapor inclusions occur mostly in Q1 and Q2 quartz and are typically aligned along linear trails. They homogenize by vapor disappearance with homogenization temperatures from 206 to 339 °C and have salinities from 0 to 18 wt% NaCl equivalent.

Liquid-vapor inclusions hosted by anhydrite were measured in two B1 veins. These inclusion assemblages have homogenization temperatures between 147 and 245 °C and an average salinity of 4 wt% NaCl equivalent. The liquid-vapor inclusions hosted by quartz in these veins have significantly higher homogenization temperatures (average 297 °C) and salinity (average 8.6 wt% NaCl equivalent). This is consistent with textural relationships that show anhydrite occurs as infill around quartz in these veins.

Liquid-vapor inclusions are the main inclusion type in the AA vein samples. These inclusion assemblages are hosted along linear trails in both Q1 and Q2 quartz that is inherited from older hydrothermal events, and also form clusters in younger Q3 quartz. The Q3 quartz identified in
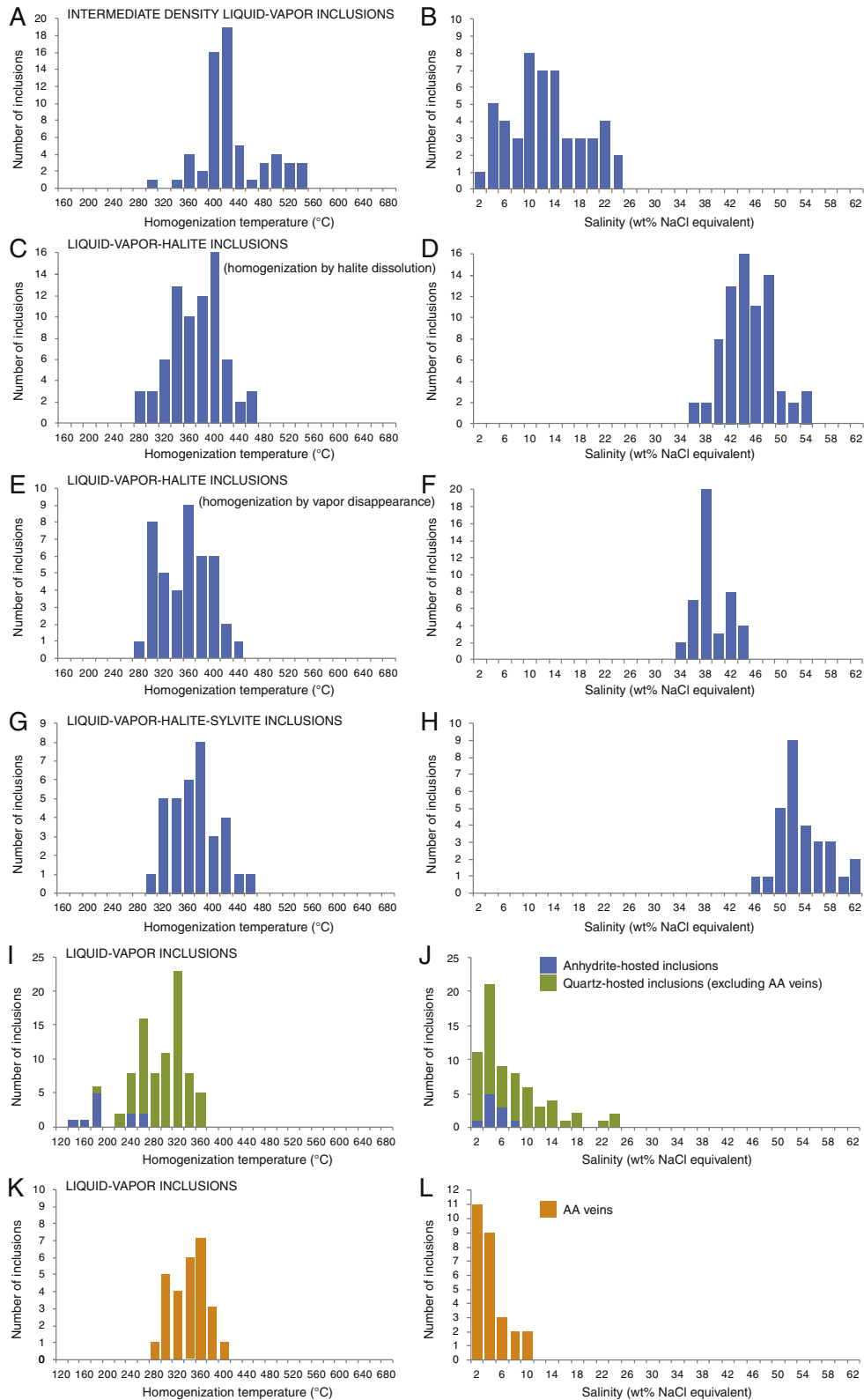
Fig. 7. Histograms of homogenization temperatures and salinity for all fluid inclusions analyzed.

AA veins is accompanied by sulfide minerals, sericite and pyrophyllite consistent with precipitation of this generation of quartz during the advanced argillic alteration event (Fig. 5C). The liquid-vapor fluid inclusion population in AA veins has homogenization temperatures that range from 291 to 356 °C and salinity that ranges from 1 to 5 wt% NaCl equivalent. This fluid is the most likely to be related to the advanced argillic alteration and mineralization event. There are two sub-populations in the temperature data, a higher temperature group centered around 340 °C and a lower temperature group centered on 300 °C.

3.6. Fluid inclusion pressure estimates

The homogenization temperature and salinity of two phase aqueous fluid inclusion assemblages (such as VL-ID, LV-ID, and LV) can be used to estimate the minimum pressure of fluid entrapment (Bodnar et al., 1985; Bodnar and Vityk, 1994; Driesner and Heinrich, 2007, Steele-MacInnis et al., 2012). A pressure correction is required to estimate the actual trapping temperature (discussed below). The highest temperature VL-ID inclusion assemblage (506 °C) is estimated to have been trapped at a minimum pressure of 600 bars (Fig. 8; Driesner and Heinrich, 2007; Steele-MacInnis et al., 2012).

A homogenous low salinity aqueous fluid that undergoes cooling and depressurization may intersect its solvus forming immiscible saline (LVH-V) and vapor-rich (VL) fluids. The homogenization temperature and salinities of the two immiscible fluids correspond to a unique set of temperature-pressure conditions that represent the trapping conditions of the fluid (Roedder and Bodnar, 1980). Although the simple brine inclusions (LVH-V) and coexisting vapor-rich inclusion assemblages identified in this study do not occur along the same inclusion trails, it is interpreted that they are the product of fluid immiscibility as both assemblages occur within the same quartz generation as identified by CL. Many studies have shown than brine and vapor fluid inclusions in porphyry deposits are the product of fluid immiscibility (e.g., Roedder, 1971, 1984; Bodnar, 1995; Rusk et al., 2008; Landtwing et al., 2010) and where these inclusion types cannot be confidently identified on a single inclusion trail it is valid to use the highest temperature brine assemblages to approximate the conditions during trapping (e.g., Hedenquist et al., 1998). The highest temperature brine inclusion assemblage measured in Type A, B and M veins (394 °C, 43 wt% NaCl equivalent) would indicate an approximate pressure of entrapment of 170 bars (Fig. 8).
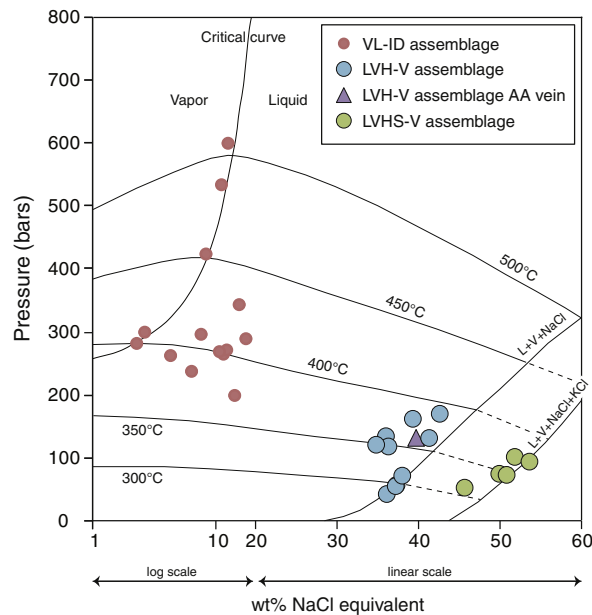
Fig. 8. Phase diagram for the system NaCl-H$_2$O (Driesner and Heinrich, 2007) showing all brine assemblages that homogenize by vapor disappearance and intermediate-density fluid inclusion assemblages that homogenize by vapor disappearance. Each point represents the average data from one assemblage of inclusions. Critical curve, two-phase surfaces and halite saturation curve (L + V + NaCl) from Driesner and Heinrich (2007). Halite-sylvite saturation curve (L + V + NaCl + KCl) estimated using halite dissolution temperatures from liquid-vapor-halite-sylvite fluid inclusions that homogenize by halite dissolution from this study. Two-phase surfaces have been extended from halite saturation curves to equivalent temperature on halite-sylvite saturation curves (dashed lines) based on pressure estimates from Sterner et al. (1988).

Brine inclusions that homogenize by halite dissolution (LVH-H), i.e., in the absence of vapor, suggest that the inclusions were either trapped at high pressure in the single-phase field (Bodnar, 1994; Cline and Bodnar, 1994), trapped a halite-saturated brine at very low pressure (Eastoe, 1978; Cloke and Kesler, 1979; Wilson et al., 1980), or were modified after entrapment by water loss (Sterner et al., 1988). In these assemblages there is no obvious petrographic evidence for post-entrapment modification and vapor disappearance temperatures are constant; halite dissolution temperatures, however, can be constant or variable. This behavior could be explained by either accidental trapping of halite in a halite-saturated fluid (Lecumberri-Sanchez et al., 2015) or trapping at high pressure (Becker et al., 2008). In general, these brines occur in samples from the deepest part of the deposit but when a pressure correction is applied (Becker et al., 2008; Steele-MacInnis et al., 2012) many of the calculated pressures are unrealistically high with values up to 4.6 kbars.

The assemblages of polyphase brine fluid inclusions (LVHS-V and LVHS-H) are typically associated with at least a few intermediate-density inclusions. Vapor-rich inclusions typically occur nearby but in different planes to the polyphase brine inclusions (Fig. 6J); this suggests there has been some separation of the two fluids during cooling and decompression but, as for the simple brine inclusions discussed above, they are interpreted to be the product of fluid immiscibility. In order to estimate the pressure for polyphase brines they need to be modeled in the H$_2$O-NaCl-KCl system (Sterner et al., 1988) which has been projected onto Fig. 8. An approximate pressure of formation of 100 bars is estimated for the highest temperature assemblages (Steele-MacInnis et al., 2012).

Minimum pressure estimates based on maximum homogenization temperatures and salinities for liquid-vapor (LV) inclusions related to advanced argillic alteration are 180 bars.

3.7. Summary of fluid types identified in the Pebble deposit

Table 4 summarizes the fluid inclusion data and relates the data to the evolution of quartz veins in the deposit. The highest temperature intermediate-density fluid (VL-ID) is associated with the oldest Q1 quartz in the mostly early and deepest A1, A2, B1 and B3 veins which are hosted by early, weak, sodic-potassic alteration. Intermediate-density inclusions of slightly lower temperature are commonly associated with LVH-H inclusions in Q1 and Q2 quartz in these same veins. LVH-V inclusions and coexisting vapor inclusions occur in younger B1 and M veins, as well as some B3 veins, when hosted by sodic-potassic alteration.

The more complex brines represented by LVHS-H and LVHS-V inclusions occur in Q3 quartz associated with sulfide minerals in B1 veins hosted by potassic alteration, where they also coexist with vapor-rich inclusions. The association between LVHS inclusion assemblages and Q3 quartz which is synchronous with much of the chalcopyrite precipitation (Fig. 5A and B) suggests these inclusion assemblages represent the fluid most closely related to the majority of metal precipitation.

Lower temperature, secondary LV inclusions occur in all vein types and are likely related to illite ± kaolinite alteration. Fluid inclusion relationships in veins related to advanced argillic alteration are more complex. Here some inclusions, particularly LV-ID and LVH-H inclusions in Q1 and Q2 quartz, are considered relicts of fluids related to early alteration; this is consistent with the model presented in Lang et al. (2013). The fluids more likely to be related to the advanced argillic alteration and mineralization are the abundant LV inclusions in Q3 quartz that hosts sulfide, sericite and pyrophyllite.

4. Stable isotope study

Stable isotope data were obtained for hydrothermal minerals in 46 samples from all alteration zones in the deposit (Table 1, Fig. 2). The aim of this work is to characterize the sources of fluids which formed

Table 4
Summary of fluid inclusion data.

Inclusion type	Vein association	Main quartz association	Homogenization temperature range (°C)	Salinity (wt% NaCl equivalent)		Host rock hydrothermal alteration type	Minimum pressure estimate based on highest T inclusions
				Range	Average		
VL-ID	A1, A2, B3, (B1)	Q1 > Q2	377–506	2–17	9.5	Deepest weak sodic-potassic	600 bars
LV-ID	AA	Q1	370–498	17–21	19.5	Advanced argillic	
LVH-H	A1, A2, B1, B3	Q1 = Q2	334–439	41–52	44	Deepest weak sodic-potassic	
LVH-H	AA	Q1 = Q2	299–394	38–48	42	Advanced argillic	
LVH-V	B1, M, B3	Q2	quartz dominant veins: 353–394, veins with carbonate or anhydrite infill: 281–317	quartz dominant veins: 35–43, veins with carbonate or anhydrite infill: 36–38	38 37	Sodic-potassic	170 bars
LVHS-H	B1	Q3	302–420	48–59	52	Potassic	
LVHS-V	B1	Q3	315–375	46–54	50	Potassic	100 bars
LV	A1, B1, M, B3	Q1 = Q2	206–339	0–18	6	All where overprinted by illite ± kaolinite	
LV	AA	Q3	291–356	1–5	3	Advanced argillic	180 bars
LV ANH	B1		147–245	3–4	4	Deepest weak sodic-potassic	

the Pebble deposit. The isotopic results are discussed for each alteration zone below.

4.1. Sample selection and analytical methods

The $\delta^{18}O$ and δD compositions were determined for 33 mineral separates that include biotite, chlorite, illite, sericite, pyrophyllite and kaolinite. The $\delta^{18}O$ values were determined for 18 mineral separates that include quartz, K-feldspar, albite, magnetite, ankerite, and anhydrite. Samples used for mineral separates were analyzed by a SEM with mineral mapping capabilities (Gregory et al., 2013) and the maps were used to identify areas of the target mineral which was then separated using a microdrill. The purity of the mineral separates was confirmed using short-wave infrared analysis and XRD on the same aliquot as used for stable isotope analysis. All isotope results are given in Table 5.

All isotope analyses were run at GNS Science, Gracefield, New Zealand. Isotopic ratios are reported relative to VSMOW. Oxygen isotopic ratios in silicate and magnetite separates were measured using a CO_2 laser-based fluorination line (BrF5 reagent). Samples were heated overnight to 150 °C prior to loading into the vacuum extraction line. Oxygen isotopic ratios in carbonate separates were analyzed on a GVI IsoPrime Carbonate Preparation System at a reaction temperature of 60 °C and run via dual inlet on the IsoPrime spectrometer. The precision on all $\delta^{18}O$ values is 0.15‰. Deuterium isotopic ratios in hydrosilicate separates were measured as H_2 gas after samples were pyrolyzed at 1450 °C in silver capsules. Deuterium was analyzed on a HEKAtech high-temperature elemental analyzer coupled with a GV Instruments IsoPrime mass spectrometer. The precision on the δD data is 1.5‰.

4.2. Temperature estimates for isotope equilibrium calculations of hydrothermal fluid composition

The isotopic composition of fluid in equilibrium with the different analyzed minerals is calculated using the fractionation equations in Table 2 and the temperatures estimated using fluid inclusion microthermometry (Table 4) and mineral stability data. The calculated fluid compositions are shown in Table 5 and presented graphically in Fig. 9.

Sodic-potassic and potassic alteration are high temperature assemblages that likely formed over a range of temperatures starting with wall rock reactions with the initial single-phase hydrothermal fluid at >600 °C and continuing via reaction with brine and vapor fluid types as cooling and depressurization occurs down to temperatures of 350 °C (Eastoe, 1978; Khashgerel et al., 2006; Seedorff et al., 2005; Sillitoe, 2010). Using the approach of Hedenquist et al. (1998), the maximum temperature of brine inclusion assemblages in each zone is used for stable isotope calculations; 400 °C for sodic-potassic alteration minerals and 375 °C for potassic alteration minerals. Temperatures of 300 °C and 190 °C are used for calcite and anhydrite, respectively, based on fluid inclusion data directly related to these minerals.

Illite has a stability range of 250 to 300 °C and kaolinite is stable at temperatures <280 °C (Seedorff et al., 2005). Chlorite has a similar temperature range of 200 to 300 °C (Khashgerel et al., 2006). Aqueous fluid inclusion assemblages found throughout the deposit that have a temperature range of ~200 to 340 °C with the majority clustering around 280 °C are likely related to this low temperature alteration. Therefore, 280 °C is estimated as the temperature for all samples of illite, kaolinite and chlorite as well as one sample of sericite from the edge of the deposit.

Sericite and pyrophyllite from the advanced argillic alteration zone are stable across a similar temperature range of 280 to 360 °C based on minerals stability data (Hemley et al., 1980; Watanabe and Hedenquist, 2001; Seedorff et al., 2005). Fluid inclusion data presented here suggest fluids associated with advanced argillic alteration range from ~290 to 360 °C. As the fluid inclusion data is bimodal with peaks

Table 5
Stable isotope data.

| Sample number	Sample location	Mineral	Temperature[a] (°C)	Measured		Fluid composition[b]	
				δ^{18}O mineral (‰ VSMOW)	δD mineral (‰ VSMOW)	δ^{18}O fluid (‰ VSMOW)	δD fluid (‰ VSMOW)
Sodic-potassic alteration							
6338-3100	Sodic-potassic zone	Biotite	400	4.7	−124	6.8	−74
6338-3800		Biotite		7.2	−115	9.3	−65
11527-479.7		Biotite		6.9	−96	9.0	−46
11527-2668.2		Biotite		4.1	−115	6.2	−65
8412-4594		K-feldspar		−6.4		−9.2	
11529-2338.5		K-feldspar		9.2		6.4	
11527-1601		Albite		10.5		7.1	
11531-1272.5		Magnetite		5.3		12.2	
7399M-286		Magnetite		1.9		9.8	
8427M-812.5		Magnetite		0.2		8.1	
8431M-358		Magnetite		3.0		10.9	
8432M-134		Magnetite		2.2		10.1	
7392M-1107.5		Quartz		11.1		6.0	
8426M-714		Quartz		9.9		4.8	
11531-1272.5		Quartz		10.9		5.8	
7397M-451		Ankerite		15.3		10.8	
7399M-286		Ankerite		17.4		12.9	
8439M-561		Ankerite		14.1		9.6	
7392M-1107.5		Calcite	300	7.5		−0.1	
8426M-714		Calcite		5.8		−1.7	
11529-2244		Anhydrite	190	9.0		−1.2	
11529-2481		Anhydrite		8.9		−1.3	
Potassic alteration							
8401-3077	Potassic zone	Biotite	375	0.0	−115	1.9	−61
7366-2723		Biotite		0.5	−116	2.4	−63
7366-3310		Biotite		−3.5	−125	−1.6	−71
7367-3253		Biotite		−2.7	−119	−0.8	−66
Quartz-illite-pyrite and quartz-sericite-pyrite alteration							
8430-461	Quartz-sericite-pyrite zone	Sericite	280	8.2	−92	4.1	−67
7395M-490	Quartz-illite-pyrite	Illite		6.8	−101	2.7	−76
7395M-371	zone	Illite		7.1	−92	3.0	−67
4231-155		Illite		7.4	−97	3.3	−72
Illite ± kaolinite alteration							
11529-2338.5	Sodic-potassic zone	Illite	280	6.2	−96	2.1	−71
8430-4107		Illite		7.4	−100	3.3	−75
11531-1412.5		Illite		8.4	−93	4.3	−68
7385-2854	Potassic zone	Illite		−5.0	−126	−9.1	−101
7379-2387		Illite		−4.6	−126	−8.7	−101
7360-3357		Illite		−0.7	−122	−4.8	−97
6354-3110	Quartz-sericite-pyrite	Illite		−2.8	−115	−6.9	−90
6354-3068	zone	Illite		−2.0	−117	−6.1	−92
11527-890	Sodic-potassic zone	Kaolinite		7.2	−106	4.9	−91
7375-3497		Chlorite		−6.6	−126	−7.1	−87
Advanced argillic alteration							
7374-1936	Advanced argillic alteration zone	Sericite	340	9.1	−133	6.5	−108
7374-2075		Sericite		7.2	−130	4.6	−105
7386-2552		Sericite		8.6	−127	6.0	−102
7387-3606		Sericite		−6.3	−135	−8.9	−110
7387-3035		Sericite-illite		−4.1	−131	−6.7	−106
8415-3216		Pyrophyllite	300	1.2	−121	−3.7	−96
8412-3968		Pyrophyllite		0.5	−121	−4.4	−96
8412-4009		Pyrophyllite		1.0	−124	−3.9	−99
7378-2954		Pyrophyllite		4.3	−135	−0.6	−110
8422-2919		Pyrophyllite		2.0	−133	−2.9	−108
7381-2073		Pyrophyllite		−0.6	−134	−5.5	−109

[a] See text for explanation of temperatures used.
[b] Fluid composition in equilibrium with mineral calculated using isotope fractionation equations listed in Table A2.

at 340 and 300 °C and as pyrophyllite is paragenetically later than sericite, temperatures of 340 and 300 °C are estimated for sericite and pyrophyllite, respectively.

4.3. Sodic-potassic alteration

Isotopic compositions were determined for biotite, albite, K-feldspar, ankerite, magnetite, quartz and anhydrite from samples with sodic-potassic alteration. The measured isotopic compositions for biotite from EB veins and wall rock alteration range from +4.1 to +7.2 per mil δ^{18}O and −124 to −96 per mil δD. Using a temperature of 400 °C, the calculated δ^{18}O and δD composition of water in equilibrium with the biotite ranges from +6.2 to +9.3 and −74 to −46 per mil, respectively. The measured δ^{18}O values for albite and K-feldspar separates (excluding one outlier) range from +9.2 to +10.5 per mil corresponding to calculated δ^{18}O values in the fluid of +6.4 to +7.1
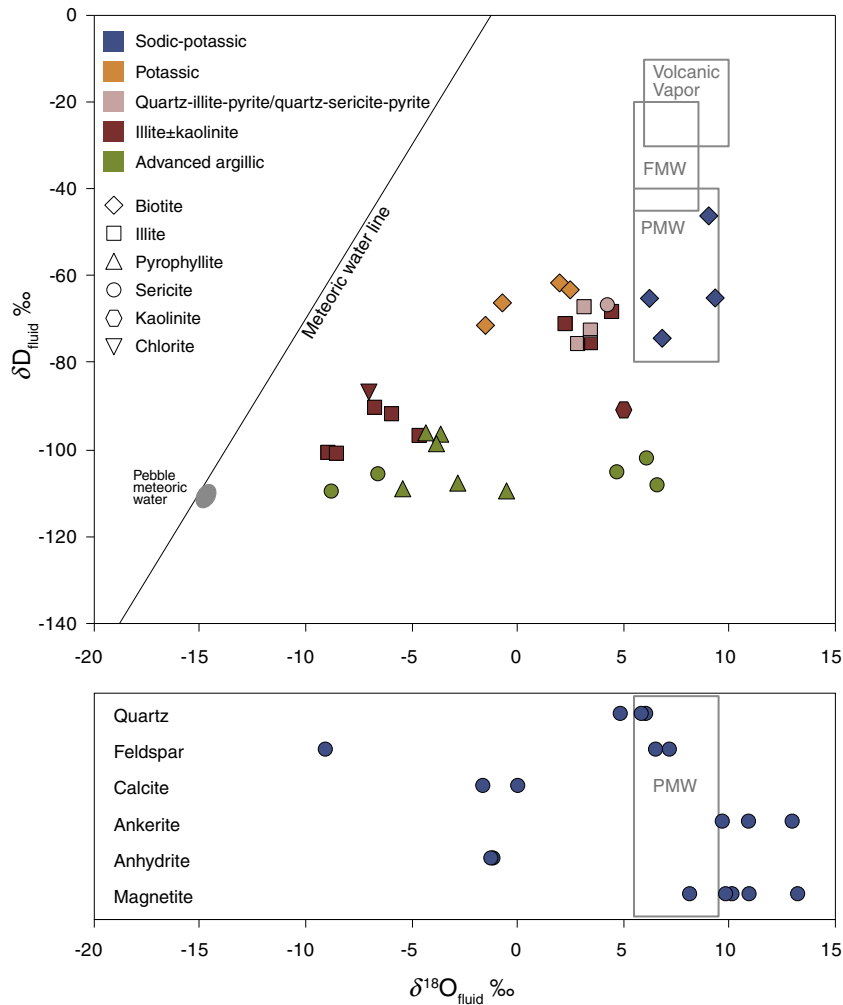
Fig. 9. Calculated $\delta^{18}O$ and δD values for hydrothermal fluids in equilibrium with various minerals that form part of the alteration assemblages present in the Pebble deposit. Meteoric water line (Craig, 1961), FMW - felsic magmatic water (Taylor, 1992), PMW - primary magmatic water (Taylor, 1974), volcanic vapor (Giggenbach, 1992), Pebble meteoric water (L. Monk, pers. comm. 2011). Temperatures used for calculation taken from fluid inclusion data as follows: sodic-potassic - 400 °C (except calcite - 300 °C and anhydrite - 190 °C), potassic - 375 °C, quartz-illite/sericite-pyrite - 280 °C, illite ± kaolinite - 280 °C, advanced argillic sericite - 340 °C, advanced argillic pyrophyllite - 300 °C. Data presented in Table 5.

per mil which overlaps with the range of values found for biotite. These results plot in the primary magmatic water field of Taylor (1974) suggesting that magmatic fluids are related to sodic-potassic alteration (Fig. 9). The measured $\delta^{18}O$ values for ankerite separates range from +14.1 to +17.4 per mil $\delta^{18}O$ and magnetite separates range from +0.2 to +5.3 per mil corresponding to calculated $\delta^{18}O$ values in the fluid of +8.1 to +12.9 per mil. These results overlap with the top of the range of values found for biotite and extend to values heavier than primary magmatic water (Fig. 9).

The measured $\delta^{18}O$ values for quartz from B1, M and B3 veins range from +9.9 to +11.1 per mil corresponding to calculated $\delta^{18}O$ values in the fluid of +4.8 to +6.0 per mil, which are slightly lower than the results for biotite and feldspar and plot just slightly to the left of the primary magmatic water field (Fig. 9). Two samples of calcite were analyzed from deep B1 and B3 veins. The fluid in equilibrium with the calcite assuming a temperature of 300 °C has an $\delta^{18}O$ signature of −1.7 to −0.1 per mil, intermediate between magmatic water and meteoric water compositions (Fig. 9). Two anhydrite samples from deep B1 veins were analyzed for $\delta^{18}O$. Using a temperature of 190 °C, the $\delta^{18}O$ value for a fluid in equilibrium with anhydrite ranges from −1.3 to −1.2 consistent with fluids that are a mixture between meteoric and magmatic fluids (Fig. 9).

4.4. Potassic alteration

Biotite from B1 veins and wall rock alteration in the potassic alteration zone has a measured isotopic composition that ranges from −3.5 to +0.5 per mil $\delta^{18}O$ and −125 to −115 per mil δD. A fluid in equilibrium with this biotite has a composition of −1.6 to +2.4 per mil $\delta^{18}O$ and −71 to −61 per mil δD using a temperature of 375 °C. This fluid has the same δD signature as the sodic-potassic alteration zone fluids, however, the $\delta^{18}O$ values are shifted to lighter values and therefore the potassic alteration fluids plot to the left of the primary magmatic water field (Fig. 9). This is similar to the trend seen in quartz from veins in the sodic-potassic alteration zone.

4.5. Quartz-illite-pyrite/quartz-sericite-pyrite and illite ± kaolinite alteration

Eleven samples of illite from a variety of alteration zones including the sodic-potassic, potassic, quartz-illite-pyrite and quartz-sericite-pyrite zones were analyzed. The measured isotopic values fall into two distinct groups. The first group contains illite that overprints the potassic

and quartz-sericite-pyrite alteration zones and has a range in measured isotopic values from -5.0 to -0.7 per mil and -126 to -115 per mil $\delta^{18}O$ and δD, respectively. A fluid in equilibrium with illite of this composition has isotopic values of -9.1 to -4.8 per mil $\delta^{18}O$ and -101 to -90 per mil δD, using a temperature of 280 °C. These fluids plot on a mixing line between primary magmatic waters and meteoric waters (Fig. 9). The data plot close to the meteoric values suggesting these waters make up a major component of the fluids responsible for illite alteration (Fig. 9). The fluid compositions trend towards values on the meteoric water line that are the same as present day values measured from streams and seeps in the deposit area that average -14.8 per mil $\delta^{18}O$ and -111 per mil δD (L. Monk, personal communication, 2011). Therefore, the meteoric water composition at the time of mineralization is assumed to be close to present day values. This is plausible because the deposit area has not significantly changed in terms of latitude since its formation based on paleomagnetic data (Goldfarb et al., 2013). Other Cretaceous deposits in Alaska have similar light $\delta^{18}O$ and δD values inferred for meteoric water compositions, e.g., Donlin Creek (Goldfarb et al., 2004).

The second group of samples includes illite that overprints sodic-potassic alteration and illite from the quartz-illite-pyrite alteration zone. These samples have measured isotopic values that range from $+6.2$ to $+8.4$ per mil $\delta^{18}O$ and -101 to -92 per mil δD. The calculated fluid composition at 280 °C has a $\delta^{18}O$ signature of $+2.1$ to $+4.3$ per mil and a δD signature of -76 to -67 per mil. This fluid plots to the left of the primary magmatic water field, and suggests that these fluids have a very significant magmatic component (Fig. 9).

One sample of kaolinite was analyzed from the sodic-potassic zone. It returned $+7.2$ per mil $\delta^{18}O$ and -106 per mil δD, consistent with a fluid composition of $+4.9$ per mil $\delta^{18}O$ and -91 per mil δD at 280 °C, the same fluid oxygen composition as the illite samples from the sodic-potassic alteration zone but significantly lighter deuterium (Fig. 9). One sample of sericite from the quartz-sericite-pyrite alteration returned $+8.2$ per mil $\delta^{18}O$ and -92 per mil δD and, assuming the same 280 °C temperature used for quartz-illite-pyrite alteration, gives a fluid composition of $+4.1$ per mil $\delta^{18}O$ and -67 per mil δD. This fluid composition overlaps the second group of illites which have the strong magmatic signature (Fig. 9).

One chlorite sample was analyzed and has measured isotopic values of -6.6 per mil $\delta^{18}O$ and -126 per mil δD. Assuming a temperature of 280 °C, the calculated fluid composition is -7.1 per mil $\delta^{18}O$ and -87 per mil δD. This fluid composition overlaps with the low-temperature illite samples suggesting that chlorite alteration is also a result of fluids with a large component of meteoric water (Fig. 9). Chlorite could be part of the sodic-potassic alteration assemblage so a temperature of 400 °C may be more applicable, but even at this temperature the chlorite sample still overlaps with the low-temperature illite samples.

4.6. Advanced argillic alteration

Oxygen and deuterium isotopes were analyzed in six samples of pyrophyllite and five samples of sericite from the area affected by the advanced argillic alteration overprint. The measured isotopic values range from -6.3 to $+9.1$ per mil $\delta^{18}O$ and -135 to -121 per mil δD. Using a temperature of 340 °C for sericite and 300 °C for pyrophyllite, the isotopic composition of the fluids in equilibrium with the advanced argillic alteration falls into two groups. The three sericite samples that represent the core of the sericite alteration zone are in equilibrium with a fluid composition of $+4.6$ to $+6.5$ per mil $\delta^{18}O$ and -108 to -102 δD. This fluid overlaps with magmatic fluid compositions in terms of oxygen and is significantly below the primary magmatic water field in terms of deuterium (Fig. 9).

The pyrophyllite samples, along with one sample of sericite from the pyrophyllite zone and another that is transitional to illite alteration, are in equilibrium with a slightly different fluid composition with a range of values from -8.9 to -0.6 per mil $\delta^{18}O$ and -110 to -96 per mil δD. This fluid has the same deuterium signature as the sericite alteration fluids but lower oxygen isotopic values that are shifter towards the Pebble meteoric water composition suggesting mixing between the fluids that produced the sericite alteration and meteoric water (Fig. 9).

5. Discussion

The fluid inclusion and stable isotope data are combined with geological relationships to reconstruct the hydrothermal evolution of the Pebble porphyry deposit. The following discussion considers the conditions of deposit formation to better understand the processes that produced deposit scale variations in hydrothermal alteration and mineralization at Pebble.

5.1. Evolving pressure conditions and phase separation

Intermediate-density fluid inclusions have been identified in numerous porphyry Cu ± Au ± Mo deposits including Butte, Montana (Rusk et al., 2008), Bingham Canyon, Utah (Landtwing et al., 2010) and many others (Audétat et al., 2008). These intermediate-density fluids have been interpreted to represent a single-phase aqueous magmatic parent fluid that exsolved from fractionating magma, transporting the metals and sulfur necessary to form porphyry style mineralization. The intermediate-density fluid inclusions (VL-ID) at Pebble are similarly interpreted to represent the parental fluid that exsolved from magma at depth.

The pressure of emplacement of the Kaskanak Batholith has been estimated using Al-in-amphibole geobarometry (Olson, 2015). That study found that the equigranular granodiorite below the east zone of the Pebble deposit represents a paleodepth of 3.8 km, which suggests pressure conditions of ~1 kbar under lithostatic conditions. Pressures estimate using the Al-in-amphibole geobarometer are ±0.6 kbars (Anderson and Smith, 1995), however, in this case the errors are estimated to be less. The minimum pressure of 600 bars for intermediate-density fluid inclusions presented herein was estimated from samples at approximately the same paleodepth as the sample used for geobarometry. A maximum pressure can be estimated for the intermediate-density fluid based on the highest probable temperature of exsolution from the intrusive source of 700 °C. This maximum pressure would be 1.4 kbars. So errors on the geobarometry of ±0.4 kbars are more likely and translate to a depth error of ±1.5 km. As the majority of porphyry deposits occur at depths <4 km (Sillitoe, 2010), a depth of ~3.8 km at the base of the deposit is reasonable. Based on this depth, a pressure correction of ~100 °C to the homogenization temperatures of the intermediate-density fluid inclusions (Steele-MacInnis et al., 2012) indicates trapping temperatures of the parental fluid between ~480 and 610 °C.

The presence of both brine-rich and vapor-rich fluid inclusions in almost all quartz veins analyzed suggests that the parental fluid underwent phase separation during cooling and ascent. Phase separation resulted in high-salinity simple brines (LVH-V 35–43 wt% NaCl equivalent) and very high-salinity polyphase brines (LVHS-V 46–59 wt% NaCl equivalent) that occur dominantly in quartz veins hosted by sodic-potassic and potassic alteration, respectively (Table 4). The different salinity characteristics suggest phase separation has taken place under different temperature and pressure conditions across the deposit. Pressure estimates for brines in quartz veins hosted by sodic-potassic alteration are 170 bars compared with 100 bars for brines in quartz veins hosted by potassic alteration. The samples from the two alteration zones represent similar paleodepths in the deposit so the differences more likely reflect

differing pressure regimes as a function of proximity to the fluid source (discussed below). Other salt systems such as H_2O-$CaCl_2$ and H_2O-$MgCl_2$ plot at much lower pressures for the same temperature and salinity when compared to the H_2O-$NaCl$ and H_2O-KCl systems (Liebscher, 2007). Therefore, addition of other salts as suggested by first melting temps in both LVH-V and LVHS inclusions means pressure estimates could be underestimated by 100 bars at 350 to 400 °C (Liebscher, 2007; Landtwing et al., 2010); however, the relative pressure difference between the two fluid types should still be realistic (Landtwing et al., 2010).

Advanced argillic alteration overprints potassic alteration in the east part of the deposit. The minimum pressure estimate for hydrothermal fluids interpreted to be associated with advanced argillic alteration is 180 bars. It is difficult to estimate the pressure conditions under which these fluids were trapped, however, the minimum and trapping pressures may not have been significantly different given the consistency between temperatures suggested by mineral stabilities and the fluid inclusion data. Therefore, no pressure correction is applied to the advanced argillic fluids.

5.2. Magmatic-hydrothermal fluid evolution

5.2.1. High-temperature alteration and mineralization

At Pebble the initial high-temperature parental fluid cooled from over 600 °C and decompressed from approximately 1 kbar to <200 bars, which resulted in phase separation. The resulting saline brines and low-density vapor interacted with the surrounding country rocks to form sodic-potassic and potassic alteration and associated Cu-Au-Mo mineralization (Fig. 10A).

Stable isotope data from hydrothermal minerals implicate a magmatic fluid source for both sodic-potassic and potassic alteration assemblages. As the alteration progressed from sodic-potassic to potassic assemblages the $\delta^{18}O$ signature of the hydrothermal fluids evolved to lighter compositions. Mixing with meteoric waters is considered unlikely because the shift is not towards the δD values of −111 per mil, the meteoric water composition inferred for the time of mineralization (Fig. 9). This shift more plausibly reflects increased fluid-wall rock interaction (Taylor, 1974; Harris et al., 2005), quite possibly due to precipitation of isotopically-heavy quartz during hydrothermal alteration (e.g., Zheng, 1993a). A similar interpretation was invoked by Harris et al. (2005) at the Bajo de la Alumbrera Cu-Au porphyry deposit to explain a comparable trend towards lighter $\delta^{18}O$ fluid compositions which could not be attributed to mixing with meteoric water.

Increasing fluid-wall rock interaction as the hydrothermal system evolved is also suggested by the $\delta^{18}O$ signature of fluids that are enriched relative to magmatic water and which precipitated magnetite and ankerite. The magnetite and ankerite are from M and C veins which cut diorite and flysch affected by sodic-potassic alteration. The data suggest that the fluid has interacted with the diorite and has evolved to higher $\delta^{18}O$ compositions through isotopic exchange with the wall rocks. This is consistent with the intimate spatial association of M veins with the diorite, which has been interpreted to reflect availability of iron from the wall rock.

The deeper parts of the east zone are characterized by sodic-potassic alteration that also has a calcic component represented by epidote and calcite accompanied by hematite and chlorite. Stable isotope data from chlorite, however, indicates that the calcic component of the alteration is a result of fluids with a large component of meteoric water. Other isotope data for samples in this area are consistent with magmatic fluids forming the sodic-potassic component of the alteration. Therefore, the calcic component of sodic-potassic alteration may be an overprint, more akin to propylitic alteration, by low-temperature fluids with a significant meteoric water content upon early sodic-potassic alteration which formed from magmatic fluids.

In porphyry deposits some vein types can form across different hydrothermal alteration events (Seedorff et al., 2005), although most studies have found that early quartz veins such as type A and B veins are mainly formed during potassic alteration (Seedorff et al., 2005; Sillitoe, 2010). In the case of Pebble where there are both high temperature sodic-potassic and potassic alteration rather than the more typical potassic only alteration the data suggest that the type A and B veins formed throughout both alteration events. Based on fluid inclusion evidence, these quartz veins were precipitating starting at 600 °C, based on the highest temperature parental fluid, down to 375 °C, the highest temperature before quartz starts to dissolve due to its retrograde solubility (Fournier, 1985). A temperature of 375 °C is also that found for very high-salinity polyphase brines that occur in quartz spatially associated with the main stage of sulfide precipitation that occurs within the space created by quartz dissolution. Therefore, it could be interpreted that these very high-salinity brines and their associated low-density vapors are directly related to the main stage of mineralization in the deposit. These brine inclusions are only found in quartz veins that occur within the potassic alteration zone. Although simple brine inclusions have a very similar temperature range as the polyphase brines, they occur in quartz that has no spatial association with significant sulfide precipitation, and most typically, in quartz veins that are hosted by weakly mineralized sodic-potassic alteration.

Sulfide mineralization at Pebble precipitated late in the parageneses of early vein types, as is typically the case in porphyry deposits (e.g., Redmond et al., 2004; Rusk et al., 2008). Based on fluid inclusion data and quartz solubility temperatures, mineralization at Pebble formed between 375 and 330 °C. The occurrence of gold as inclusions within hydrothermal K-feldspar supports an interpretation that potassic alteration was continuing throughout the window of sulfide precipitation and also explains the strong spatial association between zones of intense potassic alteration and higher grade Cu-Au mineralization.

Vein density varies across the deposit (Lang and Gregory, 2012). Higher vein densities occur in the east of the deposit compared with the west. Higher vein densities imply higher fracture permeability resulting in lower fluid pressures and higher fluid:rock ratios. Under these conditions higher salinity brines formed in the eastern part of the deposit relative to the west. The eastern part of the deposit is interpreted to be the strongest hydrothermal center in the system where very high vein density, potassic alteration, the highest grade mineralization, the area affected by brittle-ductile deformation and the largest of the granodiorite intrusions generally coincide. The sodic-potassic alteration in the west, in contrast, was a region of lower permeability with lower vein densities lateral to the eastern hydrothermal center where local conditions contributed to generally higher pressures and resulted in the formation of lower salinity brines.

The different salinity and density characteristics of the brine and vapor phases and the variations in fluid:rock ratios on each side of the deposit has likely influenced the hydrothermal alteration mineral assemblage and efficiency of metal precipitation across the deposit. Higher fluid:rock ratios would enhance metal precipitation in the east.

5.2.2. Low-temperature clay alteration

The stable isotope data indicate that magmatic fluids were important during lower temperature alteration events. The salinity of 6 wt% NaCl equivalent in the fluids related to illite alteration is most consistent with a magmatic vapor phase or intermediate-density parental-type fluid rather than a magmatic brine. Based on this interpretation there are two possible scenarios for the fluid evolution following the potassic and sodic-potassic alteration. The first is that the vapor phases that formed during the high temperature alteration stage continued to move upwards and outwards, cooling slightly and contracting to form an acidic low-salinity aqueous fluid. The less likely second option is that a new fluid pulse was released by magma at depth and evolved to the composition preserved by illite alteration due to cooling above
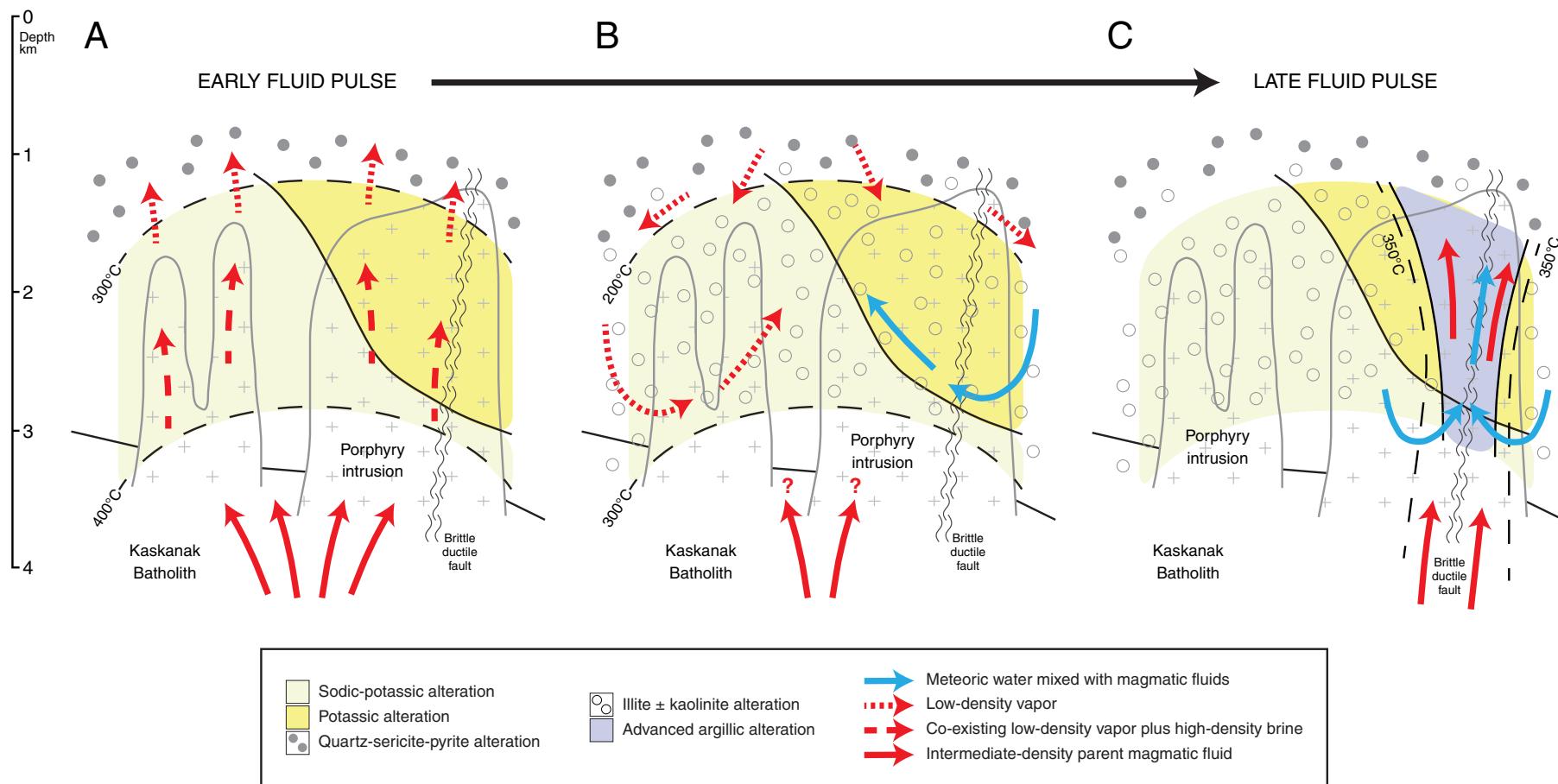
Fig. 10. Schematic evolution of fluids in the Pebble porphyry Cu-Au-Mo deposit. A. An intermediate-density, low-salinity parental fluid exsolves from crystallizing magma at depth. As this fluid flows upwards it undergoes phase separation to form co-existing brine and vapor. As these fluids cool they generate sodic-potassic and potassic alteration assemblages and associated mineralization. The vapor phase continues to ascend to shallow levels where it forms quartz-sericite-pyrite alteration around and above the deposit. B. As the system cools the vapor phase condenses and mixes with varying amounts of meteoric water. Cooling intermediate-density fluid exsolving from magmas at depth may also contribute to the fluid. This low-salinity aqueous fluid interacts with the sodic-potassic and potassic alteration assemblages and generates the overprint by illite ± kaolinite alteration assemblages. C. A new pulse of intermediate-density fluid exsolves from the same or a new magma at depth and flows along the brittle-ductile fault zone. This fluid cools above the two-phase field, so it does not undergo phase separation. This fluid interacts with pre-existing alteration types and forms sericite-rich advanced argillic alteration and high grade mineralization. As the system cools mixed magmatic-meteoric fluids flow through the center of the structure and form pyrophyllite alteration.

the two phase field therefore retaining its low salinity composition (Fig. 10B).

This fluid formed the large quartz-sericite-pyrite alteration halo around and above the potassic and sodic-potassic core of the system (Fig. 10B). With continued cooling these same fluids formed the illite ± kaolinite alteration that overprints sodic-potassic alteration and added illite to form the hybrid quartz-illite-pyrite alteration. To achieve the fluid compositions responsible for the low-temperature illite alteration that overprints the potassic and adjacent quartz-sericite-pyrite alteration, the fluid mixed with meteoric waters (Fig. 10B). Similar meteoric-rich fluid compositions were found to be responsible for illite-rich alteration at Bajo de la Alumbrera (Ulrich et al., 2002; Harris et al., 2005). Like the transition from sodic-potassic to potassic alteration, the degree of meteoric input is also a function of variable permeability across the deposit with a much larger meteoric signature associated with the higher permeability potassic core of the hydrothermal system. Only a limited amount of meteoric water was able to mix with the fluids in the less permeable sodic-potassic region.

5.2.3. Advanced argillic alteration and mineralization

Stable isotope data clearly distinguish the magmatic fluid responsible for advanced argillic alteration and mineralization from the magmatic fluid responsible for earlier sodic-potassic and potassic alteration and mineralization (Fig. 9). Low δD values for the advanced argillic alteration are best interpreted to be the result of magmatic degassing from deeper levels of the crystallizing magma chamber (Taylor, 1986), as suggested for a similar overprint documented at Oly Tolgoi (Khashgerel et al., 2009). A second potential source for this fluid is condensed magmatic volatiles as a result of the previously formed vapor phase re-entering the one phase field on isobaric cooling. Such a fluid is commonly interpreted to form advanced argillic alteration assemblages (e.g., Hedenquist et al., 1998) but in this case can be excluded as it would have a much heavier δD signature based on the isotopic compositions of the earlier fluid pulse. A third potential source of the advanced argillic fluids is mixing between low δD meteoric fluids and a fluid with the composition of the earlier magmatic fluid pulse. This is also unlikely as such a fluid would have a lighter δ18O signature correlating with the lower δD values and the fluids identified here as related to sericite-rich alteration have strongly magmatic δ18O values (Fig. 9).

The single-phase aqueous fluids that dominate the AA veins most likely represent a magmatic fluid that cooled above the two phase field (Heinrich et al., 2004; Williams-Jones and Heinrich, 2005). The fluid associated with the early high temperature alteration and the fluid associated with advanced argillic alteration could either have emanated from a single cooling and crystallizing magmatic source, or reflect fluid egress from two discrete magmatic sources. As the fluid cools below ~400 °C, disproportionation of SO2 to form H2S and H2SO4 increases its acidity (Burnham, 1979). The wall rocks would have a lack of pH buffering capacity due to previous illite alteration of feldspar, therefore, fluids would quickly evolve to the more acidic compositions required for sericite and pyrophyllite-rich alteration. As magmatic fluids cool from above 350 °C to below 300 °C and the pH decreases from 4 to 2, the resultant mineral assemblage will change from sericite-stable to pyrophyllite-stabile (Hemley and Hunt, 1992; Hedenquist et al., 1998). This process would explain the relationships seen in the Pebble deposit whereby hot hydrothermal fluids formed a zone of sericite-rich alteration and as this fluid cooled and became more spatial restricted to nearer the fluid conduit, pyrophyllite overprinted the sericite (Fig. 10C). The transition to pyrophyllite-rich assemblages occurred due to cooling as well as mixing with meteoric water. Higher sulfidation assemblages were stabilized in the sericite-rich assemblage, and as the fluid cooled and evolved into the pyrophyllite stability field, intermediate sulfidation assemblages became stable, most likely due to a decrease

in the oxygen fugacity of the fluid as a result of continued wall rock interactions (Lang and Gregory, 2012).

Overall the overprinting of advanced argillic alteration onto earlier potassic alteration can be explained by isotherm retraction whereby the heat flux from the intrusive source decreases with time resulting in a downward progression of the isotherms (Shinohara and Hedenquist, 1997; Heinrich et al., 2004). Therefore, the original region of high temperature potassic alteration is overprinted by a region of lower temperatures where sericite and pyrophyllite are stable as the system evolves through time (Fig. 10).

6. Conclusions

Fluid inclusion and stable isotope data from the Pebble porphyry Cu-Au-Mo deposit provide constraints on the magmatic-hydrothermal evolution of this giant deposit. A single-phase magmatic fluid exsolved from a magma at depth and is recorded in fluid inclusions with trapping temperatures up to 610 °C and pressures of ~1 kilobar at the base of the deposit. This parental fluid underwent phase separation under two different sets of pressure-temperature conditions that occur lateral to each other. In the eastern core of the deposit, higher vein density implies higher permeability and fluid:rock ratios, and therefore fluids were under relatively lower pressure conditions. This resulted in phase separation of the fluid to form a very high-salinity brine and a very low-density vapor. Metal precipitation from these fluids resulted in the most economically significant mineralization in the deposit which is associated with potassic alteration assemblages. Lateral to the potassic alteration, lower vein density and fluid:rock ratios resulted from lower permeability conditions and therefore higher pressure fluid conditions. Phase separation under these conditions formed relatively lower-salinity brines and low-density vapor. Metal precipitation from these fluids formed lower grade mineralization associated with sodic-potassic alteration assemblages. Mineralization occurred late in the alteration process at temperatures between 375 and 330 °C.

Following high-temperature alteration and mineralization, the vapor phase moved upward and outward, cooled, contracted and formed the unmineralized quartz-sericite-pyrite alteration halo that surrounds, and probably also occurred above, the deposit. With further cooling this fluid formed the extensive low-temperature illite ± kaolinite alteration overprint. Meteoric water was also drawn into the system at this point with meteoric signatures prominent in the fluids forming illite in the core of the system.

A second pulse of magmatic fluid followed low-temperature illite-rich alteration and formed a well-mineralized advanced argillic alteration assemblage. This magmatic fluid was also most likely a single-phase fluid whose flow was influenced by the brittle-ductile structure in the hydrothermal core of the system. This fluid did not undergo phase separation but contracted to a low-density, single-phase aqueous fluid which interacted with wall rock previously affected by potassic and illite alteration. Outside the main structure, the interaction of these fluids with wall rock resulted in sericite-rich alteration. Within the structure there was a significant influx of meteoric water resulting in pyrophyllite-rich alteration. The additional magmatic fluid pulse responsible for advanced argillic alteration and mineralization at Pebble is what makes this deposit a world class orebody.

Appendix A

Table A1
Samples used for stable isotope analysis.

Alteration zone	Sample ID	No.[a]	Sample description	Minerals for stable isotope analysis
Sodic-potassic	6338-3100	22	Sodic-potassic-altered granodiorite pluton, hydrothermal biotite replacement of igneous hornblende phenocrysts	Biotite
	6338-3800	23	Sodic-potassic-altered granodiorite pluton, hydrothermal biotite replacement of igneous hornblende phenocrysts	Biotite
	7375-3497	24	Quartz-chlorite B2 vein cutting sodic-potassic altered granodiorite pluton	Chlorite
	7392M-1107.5	12	Quartz-molybdenite-calcite B3 vein cutting weakly sodic-potassic-altered granodiorite pluton, sample also used for fluid inclusion work	Quartz, calcite
	7397M-451	25	Ankerite-pyrite-chalcopyrite-quartz C vein with alteration envelope cutting sodic-potassic-altered sediment	Ankerite
	7399M-286	1	Quartz-magnetite-ankerite M vein cutting sodic-potassic-altered diorite with kaolinite overprint, sample also used for fluid inclusion work	Magnetite, ankerite
	8412-4594	26	K-feldspar flooded sodic-potassic-altered granodiorite pluton	K-feldspar
	8426M-714	27	Quartz-calcite-pyrite-chalcopyrite B1 vein cutting sodic-potassic-altered granodiorite pluton	Quartz, calcite
	8427M-812.5	28	Magnetite-rich M vein cutting sodic-potassic-altered diorite	Magnetite
	8430-4107	29	Sodic-potassic-altered granodiorite pluton with Illite-altered K-feldspar phenocrysts	Illite
	8432M-134	30	Magnetite-quartz M vein cutting sodic-potassic-altered sediment	Magnetite
	8439M-561	31	Ankerite-quartz C vein with weak alteration envelope cutting sodic-potassic-altered sediment	Ankerite
	11527-890	32	K-feldspar flooded sodic-potassic-altered diorite with large clots of kaolinite	Kaolinite
	11527-1601	33	Albite-K-feldspar-quartz A1 vein cutting sodic-potassic-altered sediment	Albite
	11527-2668.2	34	Sodic-potassic-altered granodiorite pluton, hydrothermal biotite replacement of igneous hornblende phenocrysts	Biotite
	11529-2244	35	Anhydrite-quartz B1 vein cutting sodic-potassic-altered diorite	Anhydrite
	11529-2338.5	36	Weakly sodic-potassic altered monzonite with K-feldspar phenocrysts and illite-altered plagioclase phenocrysts	K-feldspar, illite
	11529-2481	37	Quartz-anhydrite-pyrite B1 vein cutting weakly sodic-potassic-altered monzonite	Anhydrite
	11531-1272.5	38	Quartz-magnetite M vein cutting sodic-potassic-altered diorite	Magnetite, quartz
	11531-1412.5	39	Green illite-carbonate infill of C vein cutting sodic-potassic-altered diorite	Illite
	8431M-358	40	Magnetite-quartz-pyrite-chalcopyrite matrix to brecciated sedimentary clasts	Magnetite
	11527-479.7	41	Biotite EB vein cutting K-feldspar flooded sediment	Biotite
Quartz-illite-pyrite	4231-155	42	Quartz-illite-pyrite-altered granodiorite sill with large illite clots	Illite
	7395M-371	43	Quartz-illite-pyrite-altered granodiorite pluton with illite altered feldspar phenocrysts	Illite
	7395M-490	44	Quartz-illite-pyrite-altered granodiorite pluton with illite altered feldspar phenocrysts	Illite
Potassic	7360-3357	45	Potassic-altered granodiorite pluton, illite replacement of K-feldspar phenocrysts	Illite
	7366-2723	46	Quartz-biotite B1 vein cutting potassic altered granodiorite pluton	Biotite
	7366-3310	47	Quartz-biotite B1 vein cutting potassic altered granodiorite pluton	Biotite
	7367-3253	48	Potassic-altered granodiorite pluton, hydrothermal biotite replacement of igneous hornblende phenocrysts	Biotite
	7379-2387	49	Potassic-altered granodiorite pluton, illite replacement of K-feldspar phenocrysts	Illite
	7385-2854	50	Potassic-altered granodiorite pluton, illite replacement of K-feldspar phenocrysts	Illite
	8401-3077	51	Potassic-altered granodiorite pluton, hydrothermal biotite replacement of igneous hornblende phenocrysts	Biotite
Quartz-sericite-pyrite	6354-3068	52	Quartz-sericite-pyrite-altered granodiorite sill with illite altered feldspar phenocrysts	Illite
	6354-3110	53	Quartz-sericite-pyrite-altered granodiorite sill with illite altered feldspar phenocrysts	Illite
	8430-461	54	Quartz-sericite-pyrite altered granodiorite sill, sericite replaces feldspar phenocrysts	Sericite
Advanced argillic	7374-1936	55	Pervasively sericite-altered granodiorite pluton	Sericite
	7374-2075	56	Pervasively sericite-altered granodiorite pluton	Sericite
	7386-2552	57	Pervasively sericite-altered granodiorite pluton	Sericite
	7387-3035	58	Weakly sericite-altered granodiorite pluton	Sericite-illite
	7387-3606	59	Pervasively sericite-altered granodiorite pluton	Sericite
	7378-2954	60	Pervasively pyrophyllite-altered granodiorite pluton	Pyrophyllite
	7381-2073	61	Pervasively pyrophyllite-altered granodiorite pluton	Pyrophyllite
	8412-3968	62	Pervasively pyrophyllite-altered granodiorite pluton	Pyrophyllite
	8412-4009	63	Pervasively pyrophyllite-altered granodiorite pluton	Pyrophyllite
	8415-3216	64	Pervasively quartz-pyrophyllite-altered granodiorite pluton	Pyrophyllite
	8422-2919	21	Pervasively quartz-pyrophyllite-altered granodiorite pluton, sample also used for fluid inclusion work	Pyrophyllite

[a] No. refers to numbers on Fig. 2.

Table A2
Isotope fractionation equations and factors.

Isotope fractionation equations	Temperature range (°C)	Reference
Oxygen		
$10^3 \ln \alpha_{\text{pyrophyllite-H2O}} = 2.76 \times 10^6\, T^{-2} + 1.08 \times 10^3\, T^{-1} - 5.37$	0–500	Savin and Lee (1988)
$10^3 \ln \alpha_{\text{illite-muscovite-H2O}} = 2.39 \times 10^6\, T^{-2} - 3.76$	0–700	Sheppard and Gilg (1996)
$10^3 \ln \alpha_{\text{kaolinite-H2O}} = 2.76 \times 10^6\, T^{-2} - 6.75$	0–350	Sheppard and Gilg (1996)
$10^3 \ln \alpha_{\text{chlorite-H2O}} = 2.69 \times 10^9\, T^{-3} - 6.34 \times 10^6\, T^{-2} + 2.97 \times 10^3\, T^{-1}$	170–350	Cole and Ripley (1999)
$10^3 \ln \alpha_{\text{biotite-H2O}} = 3.84 \times 10^6\, T^{-2} - 8.76 \times 10^3\, T^{-1} + 2.46$	0–1200	Zheng (1993b)
$10^3 \ln \alpha_{\text{albite (and K-feldspar)-H2O}} = 4.33 \times 10^6\, T^{-2} - 6.15$	0–1200	Zheng (1993a)
$10^3 \ln \alpha_{\text{K-feldspar-H2O}} = 2.39 \times 10^6\, T^{-2} - 2.51$	400–500	Matsuhisa et al. (1979)
$10^3 \ln \alpha_{\text{anhydrite-H2O}} = 3.21 \times 10^6\, T^{-2} - 4.72$	100–550	Chiba et al. (1981)
$10^3 \ln \alpha_{\text{calcite-H2O}} = 4.01 \times 10^6\, T^{-2} - 4.66$	0–1200	Zheng (1999)
$10^3 \ln \alpha_{\text{ankerite-H2O}} = 4.12 \times 10^6\, T^{-2} - 4.62$	0–1200	Zheng (1999)
$10^3 \ln \alpha_{\text{magnetite-H2O}} = 3.02 \times 10^6\, T^{-2} - 12.0 \times 10^3 T + 3.31$	0–1200	Zheng and Simon (1991)
$10^3 \ln \alpha_{\text{quartz-H2O}} = 4.48 \times 10^6\, T^{-2} - 4.77$	0–1200	Zheng (1993a)
Hydrogen		
$10^3 \ln \alpha_{\text{pyrophyllite-H2O}} = -25 \pm 5$	120–400	Sheppard and Gilg (1996), Marumo et al. (1980)
$10^3 \ln \alpha_{\text{illite-muscovite-H2O}} = -25 \pm 5$	120–400	Sheppard and Gilg (1996), Marumo et al. (1980)
$10^3 \ln \alpha_{\text{kaolinite-H2O}} = -2.2 \times 10^6\, T^{-2} - 7.7$	0–300	Sheppard and Gilg (1996), Marumo et al. (1980)
$10^3 \ln \alpha_{\text{chlorite-H2O}} = -39.1$	200	Graham et al. (1987), Marumo et al. (1980)
$10^3 \ln \alpha_{\text{biotite-H2O}} = -21.3 \times 10^6\, T^{-2} - 2.8$	400–850	Suzuoki and Epstein (1976)

Notes: Hydrogen isotope fractionation factor for muscovite was used for pyrophyllite in absence of experimental data (Marumo, 1989); temperatures in equations are in Kelvin.

References

Anderson, J.L., Smith, D.R., 1995. The effects of temperature and fO₂ on the Al-in-hornblende barometer. Am. Mineral. 80, 549–559.

Anderson, E.D., Hitzman, M.W., Monecke, T., Bedrosian, P.A., Shah, A.K., Kelley, K.D., 2013. Geological analysis of aeromagnetic data from southwestern Alaska: implications for exploration in the area of the Pebble porphyry Cu-Au-Mo deposit. Econ. Geol. 108, 421–436.

Audétat, A., Pettke, T., Heinrich, C.A., Bodnar, R.J., 2008. The composition of magmatic-hydrothermal fluids in barren and mineralized intrusions. Econ. Geol. 103, 877–908.

Bakker, R.J., 1997. Clathrates: computer programs to calculate fluid inclusion V-X properties using clathrate melting temperatures. Comput. Geosci. 23, 1–18.

Becker, S.P., Fall, A., Bodnar, R.J., 2008. Synthetic fluid inclusions. XVII. PVTX properties of high salinity H2O-NaCl solutions (>30 wt% NaCl): application to fluid inclusions that homogenize by halite disappearance from porphyry copper and other hydrothermal ore deposits. Econ. Geol. 103, 539–554.

Bodnar, R.J., 1994. Synthetic fluid inclusions: XII. The system H2O-NaCl. Experimental determination of the halite liquidus and isochores for a 40 wt% NaCl solution. Geochim. Cosmochim. Acta 58, 1053–1063.

Bodnar, R.J., 1995. Fluid inclusion evidence for a magmatic source for metals in porphyry copper deposits. Mineralogical Association of Canada Short Course Series 23, 139–152.

Bodnar, R.J., Vityk, M.O., 1994. Interpretation of microthermometric data for H2O-NaCl fluid inclusions. In: De Vivo, B., Frezzotti, M.L. (Eds.), Fluid Inclusions in Minerals: Methods and Applications: Blacksbury. VA, Virginia Technical Institute, pp. 117–130.

Bodnar, R.J., Burnham, C.W., Sterner, S.M., 1985. Synthetic fluid inclusions in natural quartz. III. Determination of phase equilibrium properties in the system H2O-NaCl to 1000 °C and 1500 bars. Geochim. Cosmochim. Acta 49, 1861–1873.

Borisenko, A.S., 1977. Study of the salt composition of solutions in gas-liquid inclusions in minerals by the cryometric method. Sov. Geol. Geophys. 18, 11–18.

Bouley, B.A., St. George, P., Wetherbee, P.K., 1995. Geology and discovery at Pebble copper, a copper-gold porphyry system in southwest Alaska. In: Schroeter, T.G. (Ed.), Porphyry Deposits of the Northwestern Cordillera of North America. CIM Special vol. 46, pp. 422–435.

Burnham, C.W., 1979. Magmas and hydrothermal fluids. In: Barnes, H.L. (Ed.), Geochemistry of Hydrothermal Ore Deposits, 2nd edition John Wiley & Sons, New York, pp. 71–136.

Chiba, H., Kusakabe, M., Hirano, S.I., Matsuo, S., Somiya, S., 1981. Oxygen isotope fractionation factors between anhydrite and water from 100 to 550 °C. Earth Planet. Sci. Lett. 53, 55–62.

Clark, A.H., 1993. Are outsized porphyry copper deposits either anatomically or environmentally distinctive? Soc. Econ. Geol. Spec. Publ. 2, 213–283.

Cline, J.S., Bodnar, R.J., 1994. Direct evolution of brine from a crystallizing silicic melt at the Questa, New Mexico, molybdenum deposit. Econ. Geol. 89, 1780–1802.

Cloke, P.L., Kesler, S.E., 1979. The halite trend in hydrothermal solutions. Econ. Geol. 74, 1823–1831.

Cole, D.R., Ripley, E.M., 1999. Oxygen isotope fractionation between chlorite and water from 170–350 °C: a preliminary assessment based on partial exchange and fluid/rock experiments. Geochim. Cosmochim. Acta 63, 449–457.

Craig, H., 1961. Isotopic variations in meteoric waters. Science 133 (3465), 1702–1703.

Detterman, R.L., Reed, B.L., 1980. Stratigraphy, structure, and economic geology of the Iliamna quadrangle, Alaska: U.S. Geol. Den. Surv. Bull. 1368-B (86 p).

Driesner, T., Heinrich, C.A., 2007. The system H2O–NaCl. Part I: correlation formulae for phase relations in temperature–pressure–composition space from 0 to 1000 °C, 0 to 5000 bar, and 0 to 1 XNaCl. Geochim. Cosmochim. Acta 71, 4880–4901.

Eastoe, C.J., 1978. A fluid inclusion study of the Panguna porphyry copper deposit Bougainville, Papua New Guinea. Econ. Geol. 73, 721–748.

Fournier, 1985. The behavior of silica in hydrothermal solutions. Rev. Econ. Geol. 2, 45–61.

Giggenbach, W.F., 1992. Isotopic shifts in waters from geothermal and volcanic systems along convergent plate boundaries and their origin. Earth Planet. Sci. Lett. 113, 495–510.

Goldfarb, R.J., Ayuso, R., Miller, M.L., Ebert, S.W., Marsh, E.E., Petsel, S.A., Miller, L.D., Bradley, D., Johnson, C., McClelland, W., 2004. The late Cretaceous Donlin Creek gold deposit, Southwestern Alaska: Controls on epizonal ore formation. Econ. Geol. 99, 643–671.

Goldfarb, R.J., Anderson, E.D., Hart, C.J.R., 2013. Tectonic setting of the Pebble and other copper-gold-molybdenum porphyry deposits within the evolving Middle Cretaceous continental margin of northwestern North America. Econ. Geol. 108, 405–419.

Goldstein, R.H., and Reynolds, T.J., 1994, Systematics of Fluid Inclusions in Diagenetic Minerals - SEPM Short Course 31: Soc. Sediment. Geol., (199 p).

Graham, C.M., Viglino, J.A., Harmon, R.S., 1987. Experimental study of hydrogen-isotope exchange between aluminous chlorite and water and of hydrogen diffusion in chlorite. Am. Mineral. 72, 566–579.

Gregory, M.J., Lang, J.R., Gilbert, S., Hoal, K.O., 2013. Geometallurgy of the Pebble porphyry copper-gold-molybdenum deposit, Alaska: Implications for gold distribution and paragenesis. Econ. Geol. 108, 437–462.

Gustafson, L.B., Hunt, J.P., 1975. The porphyry copper deposit at El Salvador, Chile. Econ. Geol. 70, 857–912.

Gustafson, L.B., and Quiroga G., J., 1995, Patterns of mineralization and alteration below the porphyry copper orebody at El Salvador, Chile, Econ. Geol., vol. 90, pp. 2–16.

Hampton, B.A., Ridgway, K.D., Gehrels, G.E., 2010. A detrital record of Mesozoic island arc accretion and exhumation in the North American Cordillera: U-Pb geochronology of the Kahiltna basin, southern Alaska. Tectonics 29, TC4015. http://dx.doi.org/10.1029/2009TC002544 (21p).

Harraden, C.L., McNulty, B.A., Gregory, M.J., Lang, J.R., 2013. Shortwave infrared spectral analysis of hydrothermal alteration associated with the Pebble porphyry copper-gold-molybdenum deposit, Iliamna, Alaska, USA. Econ. Geol. 108, 483–494.

Harris, A.C., Golding, S.D., White, N.C., 2005. Bajo de la Alumbrera Copper-Gold Deposit: stable isotope evidence for a porphyry-related hydrothermal system dominated by magmatic aqueous fluids. Econ. Geol. 100, 863–886.

Hedenquist, J.W., Arribas Jr., A., Reynolds, T.J., 1998. Evolution of an intrusion-centered hydrothermal system: Far Southeast-Lepanto porphyry and epithermal Cu-Au deposits, Philippines. Econ. Geol. 93, 373–404.

Heinrich, C.A., Driesner, T., Stefansson, A., Seward, T.M., 2004. Magmatic vapor contraction and the transport of gold from the porphyry environment to epithermal ore deposits. Geology 32, 761–764.

Hemley, J.J., Hunt, J.P., 1992. Hydrothermal ore-forming processes in the light of studies in rock-buffered systems; II, some general geologic applications. Econ. Geol. 87, 23–43.

Hemley, J.J., Montoya, J.W., Marinenko, J.W., Luce, R.W., 1980. Equilibria in the system Al2O3-SiO2-H2O and some general implications for alteration/mineralization processes. Econ. Geol. 75, 210–228.

Kelley, K.D., Eppinger, R.G., Lang, J., Smith, S.M., Fey, D.L., 2011. Porphyry copper indicator minerals (PCIMs) in glacial till samples as an exploration tool: example from the giant Pebble porphyry Cu-Au-Mo deposit. Geochem. Explor. Environ. Anal. 11, 321–334.

Khashgerel, B., Rye, R.O., Hedenquist, J.W., Kavalieris, I., 2006. Geology and reconnaissance stable isotope study of the Oyu Tolgoi porphyry Cu-Au system, South Gobi, Mongolia. Econ. Geol. 101, 503–522.

Khashgerel, B., Rye, R.O., Kavalieris, I., Hayashi, K., 2009. The sericitic to advanced argillic transition: stable isotope and mineralogical characteristics from the Hugo Dummett porphyry Cu-Au deposit, Oyu Tolgoi district, Mongolia. Econ. Geol. 104, 1087–1110.

Landtwing, M.R., Furrer, C., Redmond, P.B., Pettke, T., Guillong, M., Heinrich, C.A., 2010. The Bingham Canyon porphyry Cu-Mo-Au Deposit. III. Zoned copper-gold ore deposition by magmatic vapor expansion. Econ. Geol. 105, 91–118.

Lang, J.R., Gregory, M.J., 2012. Magmatic-hydrothermal-structural evolution of the giant Pebble porphyry Cu-Au-Mo deposit with implications for exploration in southwest

Alaska. In: Hedenquist, J.W., Harris, M., Camus, F. (Eds.), Geology and Genesis of Major Copper Deposits and Districts of the World: A Tribute to Richard Sillitoe 16. Society of Economic Geologists Special Publication, pp. 167–186.

Lang, J.R., Gregory, M.J., Rebagliati, C.M., Payne, J.G., Oliver, J.L., Roberts, K., 2013. Geology and magmatic-hydrothermal evolution of the giant Pebble porphyry copper-gold-molybdenum deposit, Southwest Alaska, USA. Econ. Geol. 108, 437–462.

Lecumberri-Sanchez, P., Steele-MacInnis, M., Weis, P., Driesner, T., Bodnar, R.J., 2015. Salt precipitation in magmatic-hydrothermal systems associated with upper crustal plutons. Geology 43, 1063–1066.

Liebscher, A., 2007. Experimental studies in model fluid systems. Rev. Mineral. Geochem. 65, 15–47.

Marumo, K., 1989. Genesis of kaolin minerals and pyrophyllite in Kuroko deposits of Japan: implications for the origin of the hydrothermal fluids from mineralogical and stable isotope data. Geochim. Cosmochim. Acta 53, 2915–2924.

Marumo, K., Nagasawa, K., Kuroda, Y., 1980. Mineralogy and hydrogen isotope geochemistry of clay minerals in the Ohnuma geothermal area, northeastern Japan. Earth Planet. Sci. Lett. 47, 255–262.

Mathur, R., Munk, L., Nguyen, M., Gregory, M., Annell, H., Lang, J., 2013. Modern and paleofluid pathways revealed by Cu isotope compositions in surface waters and ores of the Pebble porphyry Cu-Au-Mo deposit, Alaska. Econ. Geol. 108, 529–541.

Matsuhisa, Y., Goldsmith, J.R., Clayton, R.N., 1979. Oxygen isotope fractionation in the system quartz-albite-anorthite-water. Geochim. Cosmochim. Acta 43, 1131–1140.

Meyer, C., Hemley, J.J., 1967. Wall rock alteration. In: Barnes, H.L. (Ed.), Geochemistry of Hydrothermal Ore Deposits. Rhinehart and Winston, New York, Holt, pp. 166–235.

Olson, N., 2015. The Geology, Geochronology, and Geochemistry of the Kaskanak Batholith, and Other Late Cretaceous to Eocene Magmatism at the Pebble Porphyry Cu-Au-Mo Deposit. Oregon State University, SW Alaska: Corvallis, Oregon (Unpublished M.Sc. thesis, 248 p).

Olson, N., Dilles, J., Kent, A., Gregory, M., 2013. Geochemistry and U-Pb zircon geochronology of the Kaskanak batholith, Pebble porphyry Cu-Mo-Au deposit, Alaska. Geol. Soc. Am. Abstr. Programs 47.

Pebble Limited Partnership, 2010. Updated Mineral Resource Estimate for Pebble Prospect February 1st 2010 News Release. www.Pebblepartnership.com.

Redmond, P.B., Einaudi, M.T., Inan, E.E., Landtwing, M.R., Heinrich, C.A., 2004. Copper deposition by fluid cooling in intrusion-centered systems: new insights from the Bingham porphyry ore deposit, Utah. Geology 32, 217–220.

Roedder, E., 1971. Fluid inclusion studies on the porphyry-type ore deposits at Bingham, Utah, Butte, Montana, and Climax, Colorado. Econ. Geol. 66, 98–118.

Roedder, E., 1984. Fluid Inclusions: Reviews in Mineralogy. p. 12 (646 p).

Roedder, E., Bodnar, R.J., 1980. Geologic pressure determinations from fluid inclusion studies. Annu. Rev. Earth Planet. Sci. 8, 263–301.

Rosso, K.M., Bodnar, R.J., 1995. Microthermometric and Raman spectroscopic detection limits of CO₂ in fluid inclusions and the Raman spectroscopic characterization of CO₂. Geochim. Cosmochim. Acta 59, 3961–3975.

Rusk, B.G., Reed, M.H., Dilles, J.H., 2008. Fluid inclusion evidence for magmatic-hydrothermal fluid evolution in the porphyry copper-molybdenum deposit at butte, Montana. Econ. Geol. 103, 307–334.

Savin, S.M., Lee, M., 1988. Isotope studies of phyllosilicates. Rev. Mineral. 19, 189–219.

Sebag, R., 2012. Global Gold Mines & Deposits 2012 Ranking: Natural Resource Holdings. pp. 1–29.

Seedorff, E., Dilles, J.H., Proffett Jr., J.M., Einaudi, M.T., Zurcher, L., Stavast, W.J.A., Johnson, D.A., Barton, M.D., 2005. Porphyry deposits: characteristics and origin of hypogene features. Econ. Geol. 251–298 (100th Anniversary Volume).

Shah, A., Bedrosian, P., Anderson, E., Kelley, K., Lang, J., 2009. Geophysical data used to characterize the regional setting of the Pebble porphyry deposit in southwest Alaska. Geol. Soc. Am. Abstr. Programs 41, 493.

Sheppard, S.M.F., Gilg, H.A., 1996. Stable isotope geochemistry of clay minerals. Clay Miner. 31, 1–24.

Shinohara, H., Hedenquist, J.W., 1997. Constraints on magma degassing beneath the Far Southeast porphyry Cu–Au deposit, Philippines. Journal of Petrology 38, 1741–1752.

Sillitoe, R.H., 2010. Porphyry copper systems. Econ. Geol. 105, 3–41.

Steele-MacInnis, M., Lecumberri-Sanchez, P., Bodnar, R.J., 2012. Short note: HokieFlincs_H2O-NaCl: a Microsoft Excel spreadsheet for interpreting microthermometric data from fluid inclusions based on the PVTX properties of H2O-NaCl. Comput. Geosci. 49, 334–337.

Sterner, S.M., Hall, D.L., Bodnar, R.J., 1988. Synthetic fluid inclusions. V. Solubility relations in the system NaCl-KCl-H2O under vapor-saturated conditions. Geochim. Cosmochim. Acta 52, 989–1005.

Suzuoki, T., Epstein, S., 1976. Hydrogen isotope fractionation between OH-bearing minerals and water. Geochim. Cosmochim. Acta 40, 1229–1240.

Taylor Jr., H.P., 1974. The application of oxygen and hydrogen isotope studies to problems of hydrothermal alteration and ore deposition. Econ. Geol. 69, 843–883.

Taylor, B.E., 1986. Magmatic volatiles: isotopic variations of C, H, and S. Rev. Mineral. 16, 185–226.

Taylor, B.E., 1992. Degassing of H2O from rhyolitic magma during eruption and shallow intrusion, and the isotopic composition of magmatic water in hydrothermal systems. Geological Survey of Japan Report. vol. 279, pp. 190–194.

Tracy, B.J., 2001. Geology and Ore Fluid Geochemistry of the Pebble Cu-Au Porphyry Deposit, Southwest Alaska Unpublished M.Sc. thesis The University of Georgia, Athens, Georgia (148 p).

Ulrich, T., Gunther, D., Heinrich, C.A., 2002. The evolution of a porphyry Cu-Au deposits, based on LA-ICP-MS analysis of fluid inclusions: Bajo de la Alumbrera, Argentina. Econ. Geol. 97, 1743–1774.

Watanabe, Y., Hedenquist, J.W., 2001. Mineralogic and stable isotope zonation at the surface over the El Salvador porphyry copper deposit, Chile. Econ. Geol. 96, 1775–1797.

Williams-Jones, A.E., Heinrich, C.A., 2005. Vapor transport of metals and the formation of magmatic-hydrothermal ore deposits. Econ. Geol. 100, 1287–1312.

Wilson, J.W.J., Kesler, S.E., Cloke, P.L., Kelly, W.C., 1980. Fluid inclusion geochemistry of the Granisle and Bell porphyry copper deposits, British Columbia. Econ. Geol. 75, 45–61.

Winant, A.R., 2010. Sericitic and Advanced Argillic Mineral Assemblages and Their Relationship to Copper Mineralization, Resolution Porphyry Cu-(Mo) Deposit, Superior District, Pinal County, Arizona Unpublished M.Sc thesis University of Arizona, Tucson (98p).

Zheng, Y.-F., 1993a. Calculation of oxygen isotope fractionation in anhydrous silicate minerals. Geochim. Cosmochim. Acta 57, 1079–1091.

Zheng, Y.-F., 1993b. Calculation of oxygen isotope fractionation in hydroxyl bearing silicates. Earth Planet. Sci. Lett. 120, 247–263.

Zheng, Y.-F., 1999. Oxygen isotope fractionation in carbonate and sulfate minerals. Geochem. J. 33, 109–126.

Zheng, Y.-F., Simon, K., 1991. Oxygen isotope fractionation in hematite and magnetite: A theoretical calculation and application to geothermometry of metamorphic iron formations: European Journal of Mineralogy. 3, 877–886.